Passive imaging using distributed apertures in multiple-scattering environments

2010 Inverse Problems 26 065002

(http://iopscience.iop.org/0266-5611/26/6/065002)

Inverse Problems **26** (2010) 065002 (37pp) doi:10.1088/0266-5611/26/6/065002

Passive imaging using distributed apertures in multiple-scattering environments

Ling Wang[1], **Il-Young Son**[2] **and Birsen Yazıcı**[2]

[1] College of Information Science and Technology, Nanjing University of Aeronautics and Astronautics, Nanjing, 210016, People's Republic of China
[2] Department of Electrical, Computer and Systems Engineering, Rensselaer Polytechnic Institute, Troy, NY 12180, USA

E-mail: yazici@ecse.rpi.edu

Received 26 May 2009, in final form 5 April 2010
Published 7 May 2010
Online at stacks.iop.org/IP/26/065002

Abstract

We develop a new passive image formation method capable of exploiting information about multiple scattering in the environment, as well as statistics of the objects to be imaged, additive noise and clutter, using measurements from a sparse array of receivers that rely on illumination sources of opportunity. The array of receivers can be distributed spatially in an arbitrary fashion with several hundred wavelengths apart. We use a physics-based approach to model a multiple-scattering environment and develop a statistical model that relates measurements in a given receiver to measurements in other receivers. The model is based on back-propagating measurements in a given receiver to a hypothetical target location and then forward propagating to another receiver location based on the Green's function of the background environment. We next address the imaging problem as a generalized likelihood ratio test (GLRT) for an unknown target location. The GLRT framework allows *a priori* scene, clutter and noise information to be incorporated into the problem formulation, as well as non-Gaussian data likelihood and *a priori* models. We address the spatially resolved hypothesis testing problem by constraining the associated discriminant functional to be linear and by maximizing the signal-to-noise ratio of the test statistics. We use the resulting spatially resolved test statistic to form the image. We present the resolution analysis of our imaging algorithms for free-space and a multiple-scattering environment model. Our analysis demonstrates the improvements in the point spread function and the signal-to-noise ratio of the reconstructed images when multiple scattering is exploited, as well as the potential artifacts and limitations. We present numerical experiments to demonstrate the performance of the resulting algorithms and to validate the theoretical findings.

(Some figures in this article are in colour only in the electronic version)

1. Introduction

1.1. Motivations and overview of our approach

Passive imaging is performed by using a single or multiple receivers measuring the scattered wave field from an object to be imaged due to illumination sources of opportunity. The illumination sources of opportunity could be cooperative where the information regarding the location, waveform or the bandwidth of the sources is available or non-cooperative where no such information is available. Passive imaging covers a wide range of applications including acoustic, seismic and radar imaging.

Most passive imaging techniques with the exception of [1, 2] implicitly assume a single-scattering environment and do not explicitly address the additive noise and clutter in measurements. In this paper, we develop a new passive imaging method capable of exploiting information about multiple scattering in the environment, statistics of the objects to be imaged and statistics (possibly non-stationary) of the additive noise and clutter. Our approach is applicable to both cooperative and non-cooperative sources of opportunity. We analyze the resolution of the images formed under different assumptions and present numerical simulations to demonstrate the performance of the resulting algorithms. While we focus specifically on passive radar imaging, our approach is also applicable to passive microwave, seismic or acoustic imaging.

Passive radar imaging is of particular interest in urban areas due to the increasing number of broadcasting stations, mobile phone base stations, communication and navigation satellites. However, single-scattering assumption, on which classical received signal-processing methods are based, is not valid in urban areas. In this paper, we develop a new passive image formation method capable of exploiting information about multiple scattering in the environment using measurements from a sparse array of receivers that rely on illumination sources of opportunity. The array of receivers can be distributed spatially in an arbitrary fashion with several hundred wavelengths apart. Such an array is referred to as a distributed aperture [3]. We use a physics-based approach to model wave propagation in multiple-scattering environments and develop a statistical model that relates measurements in a given receiver to measurements in other receivers. The model is based on back-propagating measurements in a given receiver to a hypothetical target location and then forward propagating to another receiver location based on the Green's function of the medium. We next formulate the imaging problem as a spatially resolved binary hypothesis testing problem using the model between the measurements at different receivers, statistics of the objects to be imaged and statistics of the additive noise and clutter. We address the spatially resolved hypothesis testing problem by constraining the associated discriminant functional to be linear and by maximizing the signal-to-noise ratio of the test statistic. We use the resulting spatially resolved test statistics to form the image. Under these design constraints, the image formation involves correlations of filtered and transformed measurements at different receivers where the filtering is determined by the statistics of the object to be imaged, clutter and noise; transformation is determined by the underlying Green's function of the background environment. While the present work is mainly focused on non-cooperative sources of opportunity, the results are extendible to passive imaging using cooperative sources of opportunity.

We perform the resolution analysis in terms of the point spread function (PSF) of the imaging operator and signal-to-noise ratio (SNR) of the resulting images. We first consider the PSF and SNR of the resulting images for two receivers and a single transmitter. This allows us to distill the important aspects of the analysis that can be readily generalized. We next extend our results to the case where there are multiple transmitters and more than two receivers. For the propagation medium, we first consider the single-scattering and next a multi-bounce,

multiple-scattering environment model. For the multiple-scattering environment, we assume that all multi-path bounces are specular reflections and therefore model the environment as a collection of mirror planes. This allows us to readily compare the PSF and SNR of the imaging operator obtained for the single-scattering environment to those for the multiple-scattering environment. For each scenario we identify the components of the PSF and SNR due to a point scatterer as well as the artifact component and analyze how each of these components varies with respect to the number of transmitters, receivers, as well as the number of multi-path bounces.

We present numerical simulations to verify the analysis and to demonstrate the performance of the passive imaging algorithms using non-cooperative sources of opportunity. We consider scenarios involving both point and extended targets in single-scattering and multiple-scattering environments.

1.2. Related work and advantages of our approach

There are two classes of passive imaging or detection approaches in the literature. The first class of works either assumes *a priori* knowledge of the transmitter-related information or estimate this information from measurements and address the passive imaging in the framework of bi-static imaging [4–16]. These works fundamentally rely on cross-correlating received measurements with a known or estimated transmitted waveform. The second class of works relies on cross-correlating the received measurements at one location with measurements at other locations [1, 2, 17–25]. This approach eliminates the need for knowledge about the transmitter location and waveform. As a result it is applicable to passive imaging using non-cooperative sources of opportunity. Our work falls into the second class of approaches.

The works in [4–10] rely on an additional receiver channel or a dedicated receiver with a direct line-of-sight to the transmitter to estimate transmitted waveforms. For example, in [11], the carrier frequency of the transmitters of opportunity is assumed to be known; in [12], the transmitted waveform is estimated from the measurements using the specific nature of the illuminator considered. In [13–16], the ground reflectivity is reconstructed within the bi-static synthetic aperture radar framework using either a ground-based or an airborne receiver. These works assume that the locations and the waveforms of the transmitters of opportunity are known. Additionally, they require receivers with high directivity.

In [18], passive imaging of stationary and moving targets based on cross-correlation of measurements from two different locations over a temporal window is considered. Several limitations of the approach including difficulties due to noise and clutter and selection of the temporal window are presented. In [19], a passive seismic (or acoustic) imaging algorithm based on cross-correlation of measurements at different pairs of geophones is developed. The cross-correlated measurements are then backprojected to reconstruct an image of the source intensity distribution. In [21] a spatio-temporal correlation-based passive synthetic aperture imaging method is presented. This method first correlates the received signals measured at different locations on the receiver flight trajectory(ies) and then applies a microlocal based filtered-backprojection method to obtain an image of the scene radiance.

In the field of seismic imaging, a coherent interferometric imaging method for random media was presented in [1, 2, 26]. This approach uses the free-space Green's function in which the speed of wave propagation is modeled as a random variable due to the 'cluttered' nature of the propagation medium. It is shown that the method provides statistically stable images for sources and reflectors in cluttered environments by back-propagating the cross-correlations of the traces computed over space-time windows. Recently, the method in [1] is applied to passive imaging in [17]. In [25] a similar cross-correlation procedure was proposed for passive

source localization which removes random components due to multiple scattering in randomly layered media.

The technique of cross-correlation of measurements at different receivers was also used in other problems. In [22–24], scattered wave fields recorded at two receivers are cross-correlated to estimate the Green's function between the two receiver locations. In [27–29], a spatial correlation technique is used for the waveform design problem. In [30], the spatial correlation of measurements of the radar clutter is used to develop a self-calibration technique for systems with a large antenna array.

Our method has the following advantages as compared to the existing passive imaging techniques: (1) unlike the previous approaches, we derive a data model suitable for passive distributed sparse arrays which relates the statistics of measurements at a given receiver to the statistics of the measurements at other receivers, as well as the Green's function of the background environment. This model allows us to exploit multiple scattering, as well as *a priori* noise, clutter and target statistics. With the exception of [1] and [2], existing passive imaging techniques rely on the single-scattering assumption [4–16, 18–24, 31]. (2) Unlike the previous approaches in [1, 2, 32], our imaging method is formulated in an estimation-theoretic framework, specifically as a generalized likelihood ratio test (GLRT). The GLRT is a powerful framework for beamforming and imaging in the presence of unknown parameters [33, 34]. We formulate the imaging problem as a binary hypothesis test with an unknown target location. The GLRT is a particularly suitable framework for the sparse arrays due to a limited aperture available. In the GLRT framework one attempts to extract a test statistic (a sufficient statistics of the unknown quantity of interest) as opposed to reconstructing the quantity itself since only a limited number of measurements is available. Furthermore, the GLRT formulation allows incorporation of *a priori* information on the additive noise, clutter and target, as well as non-Gaussian data likelihood and prior models. While the present work is focused on linear discriminant functionals for detector design, our formulation along with the statistical data model allows general design criteria to be considered. Furthermore, the estimation-theoretic approach provides quantitative methods of evaluation in terms of the PSF and the SNR of the resulting images. Note that the GLRT formulation is equivalent to backprojection/migration under Gaussian and non-informative white noise prior models and free-space propagation models. (See our prior work in [35] on the equivalence of the GLRT and backprojection.) In general, the GLRT provides a powerful framework for detection and imaging for scenarios involving limited apertures. For large or synthetic apertures, see [21] for the filtered-backprojection type approach. (3) Unlike the passive radar detection methods described in [4–16, 31], our approach does not necessarily require receivers with high directivity. (4) Our approach can be used in the presence of both cooperative and non-cooperative sources of opportunity.

1.3. Organization of the paper

The rest of our paper is organized as follows: in section 2, we present the measurement model for the multiple-scattering environment based on the Lippman–Schwinger equation. We define the statistical assumptions on the target, clutter and additive noise. In section 3, we use the measurement model described in section 2 and develop a new model that relates the statistics of the measurements at a given receiver to the statistics of the measurements at other receivers for distributed passive arrays. In section 4, we use the model in section 3 and address the passive imaging problem within the GLRT framework. In section 5, we provide specific examples of passive imaging for the free-space and a multi-bounce Green's function models. In section 6, we present the resolution analysis for different propagation

Table 1. Definition of variables, operators and functions.

Symbol	Designation	Symbol	Designation
$g(\mathbf{x}, \mathbf{y}, t)$	Green's function representing the field generated at location $\mathbf{x}$ and time t due to an impulsive source at location $\mathbf{y}$ at time zero	$s(\mathbf{x}, t)$	Source at location $\mathbf{x}$ and time t
E^{in}	The incident field	E^{sc}	The scattered field
V	Ground reflectivity function	T	Target reflectivity function
$\overline{T}$	Mean value of the target reflectivity function T	R^T	Autocovariance function of the target reflectivity function T
C	Clutter reflectivity function	n_C	Measurements due to clutter
n	Additive white thermal noise	$\tilde{n}$	Sum of the measurements due to clutter and noise
$R_{\tilde{n}}$	Autocovariance function of $\tilde{n}(t)$	W_s	Spatial windowing function centered at a hypothetical target location
$\hat{m}_i^j$	Measurement at the ith receiver modeled in terms of the measurement at the jth receiver	$\hat{\tilde{n}}_i$	Sum of the measurements due to clutter and noise at the ith receiver
$\mathcal{G}_{\boldsymbol{y},i}$	Forward-propagation operator from a hypothetical target location $\boldsymbol{y}$ to a receiver i	$\mathcal{G}_{\boldsymbol{y},j}^{-1}$	Back-propagation from the jth receiver to a hypothetical target location $\boldsymbol{y}$
$\mathbf{G}_{\boldsymbol{y}}$	Diagonal matrix with the elements $\mathcal{G}_{\boldsymbol{y},i}\mathcal{G}_{\boldsymbol{y},j}^{-1}$, $i = 1, \ldots, N$ and $i \neq j$, for some $1 \leqslant j \leqslant N$	$S_n^i(\omega)$	The power spectral density function of the measurements due to clutter and additive noise at the ith receiver
$\mathbf{m}$	Vector of the measurement model (see (24))	$\mathbf{m_r}$	Vector of reference measurements (see (25))
$\mathbf{R}_T$	Autocovariance matrix of $\mathbf{m}_\mathbf{r}^{(0)}$ where $\mathbf{m}_\mathbf{r}^{(0)}$ is the vector of the noise- and clutter-free reference measurements (see (35))	$\mathbf{n}$	Vector of the sum of measurements due to clutter and noise
$\mathbf{R_n}$	Autocovariance matrix of $\mathbf{n}$	$\lambda(\boldsymbol{y})$	Test statistic at location $\boldsymbol{y}$
$\mathbf{w}$	Template for a linear detector	SNR_λ	Signal-to-noise ratio of the test statistic

models and different number of receivers and transmitters. In section 7, we present numerical simulations. Section 8 concludes our discussion. Appendix A includes the derivation of the optimal linear discriminant functional used for passive image formation. Appendix B includes the derivations of the PSF and SNR for a variety of scenarios considered in sections 5 and 6.

2. Models for incident and scattered field and target, clutter and noise in multiple-scattering environments

2.1. Notational conventions

We reserve $\mathbf{x}$ to denote the location in 3D Euclidean space and $\boldsymbol{x}$ to denote the location in 2D space. We denote operators ($\mathcal{K}, \mathcal{G}, \mathcal{R}$, etc) with calligraphic letters. For a function f, $\hat{f}$ denotes its Fourier transform and f^* denotes its complex conjugate. The bold font denotes vector quantities. The non-bold italic font denotes scalar quantities. For a vector $\mathbf{m}$, $\mathbf{m}^H$ denotes its Hermitian transpose. For a detailed list of notation used throughout the paper, see table 1.

2.2. Models for the incident and scattered field in multiple-scattering environments

The propagation of electromagnetic waves in a medium due to the distribution of sources can be adequately described by the scalar wave equation [36–38]:

$$\left(\nabla^2 - \frac{1}{c^2}\partial_t^2\right) E(\mathbf{x}, t) = s(\mathbf{x}, t) \tag{1}$$

where c is the speed of electromagnetic waves in the medium, $E(\mathbf{x}, t)$ is the electric field and $s(\mathbf{x}, t)$ is the source term, at location $\mathbf{x} \in \mathbb{R}^3$ and time $t \in \mathbb{R}^+$. The propagation medium is characterized by the *Green's function* satisfying

$$\left(\nabla^2 - \frac{1}{c^2}\partial_t^2\right) g(\mathbf{x}, \mathbf{y}, t, \tau) = \delta(\mathbf{x} - \mathbf{y})\delta(t - \tau). \tag{2}$$

In this paper, we assume that the medium is stationary, i.e. g is time-invariant eliminating the fourth variable in (2). Thus, the incident field due to an arbitrary source distribution $s(\mathbf{x}, t)$ can be modeled as

$$E^{\text{in}}(\mathbf{x}, t) = \int g(\mathbf{x}, \mathbf{y}, t - \tau) s(\mathbf{y}, \tau)\, \mathrm{d}\mathbf{y}\, \mathrm{d}\tau. \tag{3}$$

In radar applications, the source term is the time-varying current density over the physical antenna aperture. For an isotropic point source located at $\mathbf{x}_0$, $s(\mathbf{x}, t) = p(t)\delta(\mathbf{x} - \mathbf{x}_0)$ where $p(t)$ is the transmitted waveform.

In the presence of inhomogeneities, the wave speed c is spatially varying. If *a priori* knowledge about the background inhomogeneity is known, c can be expressed in terms of the background propagation speed, c_b, and the perturbation due to deviation from the background reflectivity, V:

$$c^2(\mathbf{x}) = \left(\frac{1}{c_b^2(\mathbf{x})} + V(\mathbf{x})\right)^{-1}. \tag{4}$$

For typical carrier frequencies used in surveillance radar the incident field decays rapidly as it penetrates the ground [39]. We can then write $V(\mathbf{x})$ in terms of a 2D function, as in

$$V(\mathbf{x}) = V(\boldsymbol{x})\delta(x_3 - h(\boldsymbol{x})) \tag{5}$$

where $\mathbf{x} = (\boldsymbol{x}, x_3)$, $\boldsymbol{x} \in \mathbb{R}^2$ and $h : \mathbb{R}^2 \to \mathbb{R}$ represents the known ground topography.

Let E denote the total field in the medium, i.e. $E = E^{\text{in}} + E^{\text{sc}}$; then the scattered field can be modeled by the *Lippman–Schwinger equation*:

$$E^{\text{sc}}(\mathbf{x}, t) = \int g(\mathbf{x}, \boldsymbol{y}, t - \tau) V(\boldsymbol{y}) \partial_\tau^2 E(\boldsymbol{y}, \tau)\, \mathrm{d}\boldsymbol{y}\, \mathrm{d}\tau \tag{6}$$

where we define $g(\mathbf{x}, \boldsymbol{y}, t)$ as the 3D Green's function of the background environment that is equal to $g(\mathbf{x}, (\boldsymbol{y}, h(\boldsymbol{y})), t)$, $\boldsymbol{y} = (y_1, y_2)$. Note that E^{sc} appears on both sides of the equation. Thus, E^{sc} is nonlinear in V. This equation can be linearized by the first Born approximation, resulting in

$$E^{\text{sc}}(\mathbf{x}, t) \approx \int g(\mathbf{x}, \boldsymbol{y}, t - \tau) V(\boldsymbol{y}) \partial_\tau^2 E^{\text{in}}(\boldsymbol{y}, \tau)\, \mathrm{d}\boldsymbol{y}\, \mathrm{d}\tau, \tag{7}$$

which is also known as the distorted wave Born approximation (DWBA). The DWBA is valid as long as the scattering due to V is small as compared to the incident field, E^{in} [37, page 196]. We note that the DWBA is not necessary for our image formation method. However, we use the DWBA for the resolution analysis in section 6.

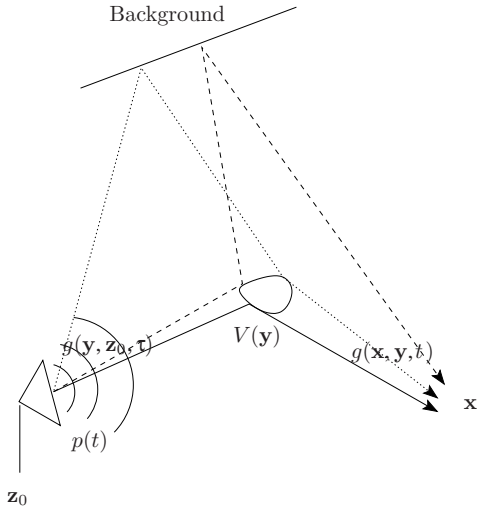

Figure 1. An illustration of the propagation of waveform $p(t)$ from the transmitter located at $\mathbf{z}_0$ to the scatterer $V(\boldsymbol{y})$ through the background medium characterized by the Green's function $g(\boldsymbol{y}, \mathbf{z}_0, t)$ and from $V(\boldsymbol{y})$ to the location $\mathbf{x}$ via $g(\mathbf{x}, \boldsymbol{y}, t)$.

Since E^{in} itself is a solution to the wave equation with $s(\mathbf{x}, t)$ as the source term, under the isotropic point antenna assumption located at $\mathbf{z}_0$, (7) can be alternatively expressed as

$$E^{\text{sc}}(\mathbf{x}, t) = \int g(\mathbf{x}, \boldsymbol{y}, t - \tau) V(\boldsymbol{y}) \partial_\tau^2 \, g(\boldsymbol{y}, \mathbf{z}_0, \tau - \tau') p(\tau') \, \mathrm{d}\tau' \, \mathrm{d}\boldsymbol{y} \, \mathrm{d}\tau \tag{8}$$

where $g(\boldsymbol{y}, \mathbf{z}_0, t)$ is the 3D Green's function defined as $g((\boldsymbol{y}, h(\boldsymbol{y})), \mathbf{z}_0, t)$ and p denotes the transmitted waveform. We note that the isotropic point antenna assumption is not necessary for the rest of our development. However, the assumption is made to simplify the rest of our discussion. If this assumption is dropped, then (8) will include an antenna beampattern term which depends on both space and time variables. Figure 1 illustrates the propagation of the transmitted signal through the background medium and scattering the incident field at $\mathbf{y}$.

2.3. Statistical models for target, clutter and noise

The above formalism allows us to utilize a physics-based model for the background, which in principle can contain an arbitrary level of details. However, it is not realistic to assume that the background model can account for arbitrarily fine scattering properties. Therefore, we determine the Green's function with respect to a known average background and model random fluctuations and unaccounted fine details as a clutter random field. This suggests that the reflectivity function V could be decomposed into two parts:

$$V = T + C \tag{9}$$

where T denotes the objects of interest called the target and C denotes heterogeneities that are neither target nor a part of the background medium, called the clutter. Such a clutter model allows us to build model mismatch into our formulation and avoid computation of the Green's function for an arbitrarily detailed environment. Note that if the arbitrarily detailed scattering properties of the background medium are known, this information can be included into the

Green's function of the background medium and the clutter model would not be needed. However, often times, it is unrealistic to obtain such information.

Furthermore, we assume that the scattered field measurements at the receiver are contaminated with additive thermal noise $n(t)$ with autocovariance function R_n. Thus, we model measurements at $\mathbf{x}_0$ as

$$m(t) = \int g(\mathbf{x}_0, \boldsymbol{y}, t-\tau) T(\boldsymbol{y}) \partial_\tau^2 E(\boldsymbol{y}, \tau)\, \mathrm{d}\boldsymbol{y}\, \mathrm{d}\tau + \tilde{n}(t) \tag{10}$$

where

$$\tilde{n}(t) = \overbrace{\int g(\mathbf{x}_0, \boldsymbol{y}, t-\tau) C(\boldsymbol{y}) \partial_\tau^2 E(\boldsymbol{y}, \tau)\, \mathrm{d}\boldsymbol{y}\, \mathrm{d}\tau}^{n_C(t)} + n(t) \tag{11}$$

and $n_C(t)$ denotes measurements due to clutter.

Without loss of generality, we assume that the measurements due to clutter are zero mean with the finite variance and autocovariance function R_{n_C}.

We assume that the additive thermal noise, $n(t)$, is white with variance σ_n^2 and is uncorrelated with $n_C(t)$. Thus, the covariance function of $\tilde{n}(t)$ is equal to

$$R_{\tilde{n}}(t, t') = R_{n_C}(t, t') + R_n(t, t') \tag{12}$$

$$= R_{n_C}(t, t') + \sigma_n^2 \delta(t - t'). \tag{13}$$

In the Fourier domain, (10) becomes

$$\hat{m}(\omega) = -\int \hat{g}(\mathbf{x}_0, \boldsymbol{y}, \omega) T(\boldsymbol{y}) \omega^2 \hat{E}(\boldsymbol{y}, \omega)\, \mathrm{d}\boldsymbol{y} + \hat{\tilde{n}}(\omega). \tag{14}$$

In this paper, we consider both deterministic and random target models. For the random target model, we assume that the target reflectivity function, $T(\boldsymbol{y})$, has finite first- and second-order statistics. The mean and the covariance functions of $T(\boldsymbol{y})$ are denoted by

$$\begin{aligned} &\mathrm{E}[T(\boldsymbol{y})] =: \overline{T}(\boldsymbol{y}) \\ &\mathrm{E}[(T(\boldsymbol{y}_1) - \overline{T}(\boldsymbol{y}_1))(T(\boldsymbol{y}_2) - \overline{T}(\boldsymbol{y}_2))^*] =: R^T(\boldsymbol{y}_1, \boldsymbol{y}_2) \end{aligned} \tag{15}$$

where E denotes the expectation operator. Furthermore, we assume that the target and clutter are mutually statistically uncorrelated.

3. A passive measurement model for distributed apertures

We define a distributed aperture as a finite collection of transmit and receive antennas that are arbitrarily located with several hundred wavelengths apart with no assumption that transmitters and receivers are colocated (see figure 2). The sparse spatial distribution of antenna elements implies that the classic delay and sum beamforming technique [40] via array processing is not applicable. Furthermore, the targets can be in the near field of the aperture. For imaging with sparse active arrays, see [3, 32, 41] and a recent survey [42] and references therein.

In the analysis that follows, we consider a sparse distribution of M transmit elements and N receive elements. In general, we assume that non-identical waveforms may be transmitted from different transmit elements. We assume that the sources of opportunity (transmitters) are non-cooperative where the location of the sources and the nature of the transmitted waveforms are not known. Therefore, the incident and scattered field models described in the previous section are not directly applicable to formulate a passive imaging method. In this section, we use the incident and scattered field models described in the previous section and derive an

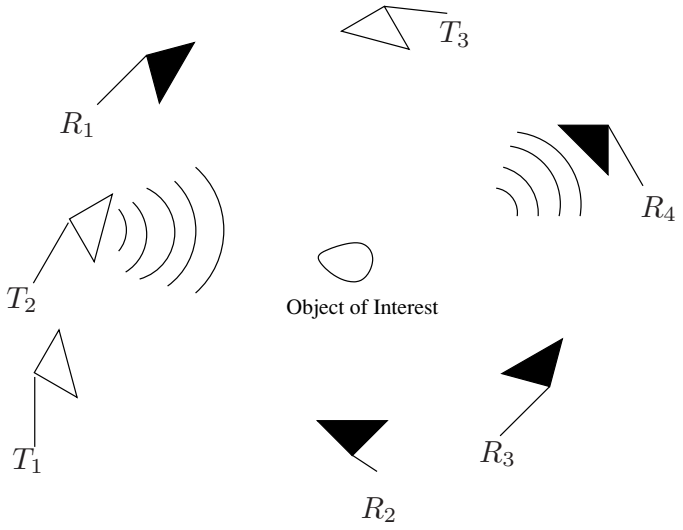

Figure 2. A typical distributed aperture setup with receive and transmit antenna elements that are several hundred wavelengths apart. The black antennas denote receive elements and the white antennas denote transmit elements.

alternative model for passive distributed arrays that relates the statistics of the measured signal at a given receiver to the statistics of the measurements at other receivers. We then use this model to formulate the passive imaging problem in the next section.

Suppose there are M transmit elements, all modeled as a point source, i.e. $s(\mathbf{x}, t) = \sum_{q=1}^{M} p_q(t)\delta(\mathbf{x} - \mathbf{z}_q)$; then the incident field at $\boldsymbol{y} \in \mathbb{R}^2$ is given by

$$E^{\text{in}}(\boldsymbol{y}, t) = \int \sum_{q=1}^{M} g(\boldsymbol{y}, \mathbf{z}_q, t - \tau)\, p_q(\tau)\, \mathrm{d}\tau. \tag{16}$$

For passive detection and imaging applications, the incident field E^{in} is not known, since the information on the transmitted waveforms and the location of the transmitters may not be available. Here, we develop an alternative measurement model that expresses measurements at each receiver in terms of the measurements at a different receiver. The model involves back-propagating the measurement at a receiver location to a hypothetical target location and then forward propagating the resulting field to another receiver location. This is illustrated in figure 3.

The forward-propagation operator is an integral operator that maps the total field and the target at a hypothetical target location $\boldsymbol{y}$ to the scattered field at the ith receiver, i.e.

$$[\mathcal{G}_{\boldsymbol{y},i} u](\omega) = \int W_s(\boldsymbol{y}', \boldsymbol{y}) \hat{g}(\mathbf{x}_i, \boldsymbol{y}', \omega) u(\boldsymbol{y}', \omega)\, \mathrm{d}\boldsymbol{y}' \tag{17}$$

$$= \int_{D_W(\boldsymbol{y})} \hat{g}(\mathbf{x}_i, \boldsymbol{y}', \omega) u(\boldsymbol{y}', \omega)\, \mathrm{d}\boldsymbol{y}'. \tag{18}$$

where $u(\boldsymbol{y}, \omega) = -T(\boldsymbol{y})\omega^2 \hat{E}(\boldsymbol{y}, \omega)$ and $W_s(\boldsymbol{y}', \boldsymbol{y})$ is a spatial windowing function of unit amplitude centered at a hypothetical target location $\boldsymbol{y}$. Note that the forward-propagation operator is $\boldsymbol{y}$ dependent due to the spatial windowing function W_s. We define the back-propagation operator as the inverse of $\mathcal{G}_{\boldsymbol{y},i}$, and denote it with $\mathcal{G}_{\boldsymbol{y},i}^{-1}$. Since the operator $\mathcal{G}_{\boldsymbol{y},i}$ is

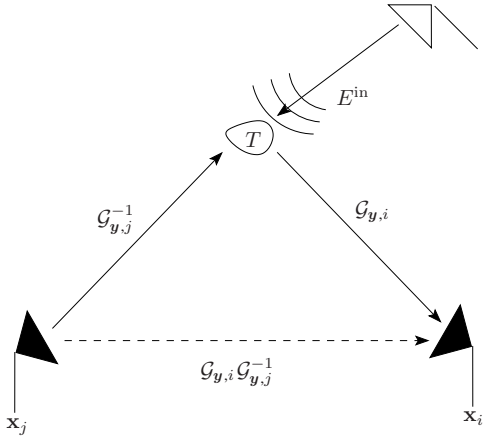

Figure 3. An illustration of the back-propagation of the scattered field at the jth receive element to a hypothetical target location and forward propagation of the total field and the target reflectivity from the hypothetical target location to the ith receive element.

applied only at a single spatial location $\mathbf{x}_i$, its inverse may not exist for all locations $\boldsymbol{y}' \in D_{W(\boldsymbol{y})}$. Thus, we replace $\mathcal{G}_{\boldsymbol{y},i}^{-1}$ with its pseudoinverse $\mathcal{G}_{\boldsymbol{y},i}^{\dagger}$ given by

$$\mathcal{G}_{\boldsymbol{y},i}^{\dagger} = \mathcal{G}_{\boldsymbol{y},i}^{*}(\mathcal{G}_{\boldsymbol{y},i}\mathcal{G}_{\boldsymbol{y},i}^{*} + \sigma\,\mathbf{I})^{-1} \tag{19}$$

where $\sigma > 0$ is a suitably chosen regularization parameter.

In an ideal scenario, where there is no noise or clutter in the measurements, we can express the ith measurement in terms of the jth measurement as follows:

$$\hat{m}_i^{j(0)}(\omega) = \mathcal{G}_{\boldsymbol{y},i}\mathcal{G}_{\boldsymbol{y},j}^{-1}\hat{m}_j^{(0)}(\omega) \tag{20}$$

where $\hat{m}_j^{(0)}(\omega)$ and $\hat{m}_i^{j(0)}$ are the noise- and clutter-free measurements at the jth and ith receivers, respectively. In the presence of noise and clutter, $\hat{\tilde{n}}_j$ is also back-propagated along with $\hat{m}_j^{(0)}(\omega)$. Therefore, if we denote $\hat{m}_j = \hat{m}_j^{(0)} + \hat{\tilde{n}}_j$, the full expression for an alternative measurement model at the ith receiver in terms of the jth measurement, i.e. $\hat{m}_i^{j}(\omega)$, becomes

$$\hat{m}_i^{j}(\omega) = \mathcal{G}_{\boldsymbol{y},i}\mathcal{G}_{\boldsymbol{y},j}^{-1}\hat{m}_j^{(0)}(\omega) + \mathcal{G}_{\boldsymbol{y},i}\mathcal{G}_{\boldsymbol{y},j}^{-1}\hat{\tilde{n}}_j(\omega) + \hat{\tilde{n}}_i(\omega) \tag{21}$$

$$= \mathcal{G}_{\boldsymbol{y},i}\mathcal{G}_{\boldsymbol{y},j}^{-1}\left(\hat{m}_j^{(0)}(\omega) + \hat{\tilde{n}}_j(\omega)\right) + \hat{\tilde{n}}_i(\omega) \tag{22}$$

$$= \mathcal{G}_{\boldsymbol{y},i}\mathcal{G}_{\boldsymbol{y},j}^{-1}\hat{m}_j(\omega) + \hat{\tilde{n}}_i(\omega). \tag{23}$$

Suppose there are N receive antennas located at $\mathbf{x}_1, \ldots, \mathbf{x}_N$, indexed by $1, \ldots, N$. A vector measurement model can be formed by taking one of the receivers as a reference. Without loss of generality, we take the jth receiver as a reference and form the following measurement vector:

$$\mathbf{m} = \begin{bmatrix} \hat{m}_1^j & \hat{m}_2^j & \cdots & \hat{m}_N^j \end{bmatrix}^T \tag{24}$$

where $\hat{m}_i^j$, $i = 1, \ldots, N$ and $i \neq j$, denotes the measurement $\hat{m}_i$ modeled in terms of the reference measurement $\hat{m}_j$. Similarly, we can vectorize the 'reference measurements', $\hat{m}_j$'s, and the measurements due to noise and clutter:

$$\mathbf{m_r} = [\hat{m}_j \quad \hat{m}_j \quad \cdots \quad \hat{m}_j]^T \tag{25}$$

$$\mathbf{n} = [\hat{\hat{n}}_1 \quad \hat{\hat{n}}_2 \quad \cdots \quad \hat{\hat{n}}_N]^T \tag{26}$$

where in $\hat{\hat{n}}_i$, $i \neq j$ as defined in (11) and (14). Note that $\mathbf{m}$, $\mathbf{m_r}$ and $\mathbf{n}$ are all vectors of length $(N-1)$.

The composition of the back-propagation and forward-propagation operators can be represented as a diagonal matrix. For non-cooperative sources of opportunity, this matrix is given by

$$\mathbf{G}_{\boldsymbol{y}} = \operatorname{diag}\left[\mathcal{G}_{\boldsymbol{y},1}\mathcal{G}^{-1}_{\boldsymbol{y},j} \quad \mathcal{G}_{\boldsymbol{y},2}\mathcal{G}^{-1}_{\boldsymbol{y},j} \quad \cdots \quad \mathcal{G}_{\boldsymbol{y},N}\mathcal{G}^{-1}_{\boldsymbol{y},j}\right] \tag{27}$$

where $i \neq j$ and $\mathbf{G}_{\boldsymbol{y}}$ is $(N-1) \times (N-1)$.

Using (21), (24)–(27), we form the vectorized passive measurement model as follows:

$$\mathbf{m}(\omega) = \mathbf{G}_{\boldsymbol{y}}\mathbf{m_r}(\omega) + \mathbf{n}(\omega) \tag{28}$$

for some range of ω. Note that in (28), all the operations are understood to be elementwise.

4. Passive target imaging as a spatially resolved binary hypothesis testing problem

We formulate the imaging problem as a binary hypothesis testing problem which has its roots in the generalized likelihood ratio test (GLRT) (see [33, 34]). The GLRT is a powerful framework for beamforming and imaging in the presence of unknown parameters. The application of the GLRT formalism to imaging involves modeling the scene as a collection of point targets with unknown locations and setting up a spatially resolved hypothesis testing problem to evaluate the presence or absence of a target [35]. The GLRT provides a particularly suitable framework for the sparse aperture arrays due to limited data available. In this formalism, we extract a spatially resolved test statistic (a sufficient statistic of the unknown quantity of interest) as opposed to reconstructing the quantity itself due to the limited number of measurements available. The image is then formed by the spatially resolved test statistic where the locations and possibly the shapes of the targets can be identified by thresholding the reconstructed image. Additionally, the GLRT framework allows us to incorporate *a priori* information on noise, clutter and target into our problem formulation. In our subsequent development, we limit ourselves to first- and second-order statistical information and constrain the discriminant functional involved in the detector design to be linear. As a result, maximizing the SNR of the test statistic gives the linear discriminant functional which is the optimal likelihood ratio test under the Gaussian assumption. In [35], we show that the GLRT under the assumptions of the free-space propagation model and white Gaussian distribution for the noise, clutter and target becomes equivalent to the backprojection approach. However, in general, the GLRT formalism can accommodate arbitrary data likelihood and prior models and can result in a nonlinear functional of the measurements.

In this section, we first set up a spatially resolved binary hypothesis testing and next determine a test statistic for each location $(\boldsymbol{y}, h(\boldsymbol{y})) \in \mathbb{R}^3$ of the scene using the measurement model developed in (28). We determine the test statistic by maximizing the SNR of the test statistic while constraining the associated discriminant functional to be linear.

The passive target detection or imaging problem can be formulated as the following spatially resolved binary hypothesis test:

$$\begin{aligned} \mathcal{H}_0 &: \quad \mathbf{m} = \mathbf{n} && \Rightarrow \text{target absent} \\ \mathcal{H}_1 &: \quad \mathbf{m} = \mathbf{G}_{\boldsymbol{y}}\mathbf{m_r} + \mathbf{n} && \Rightarrow \text{target present} \end{aligned} \tag{29}$$

where $\mathbf{G}_{\boldsymbol{y}}$, $\mathbf{m_r}$, $\mathbf{m}$ and $\mathbf{n}$ are as defined in (24)–(28).

The solution of a binary hypothesis testing problem involves design of a discriminant functional, which produces a test statistic of measurements, and a thresholding scheme [38]. To design a discriminant functional, one first needs to determine the statistics of the random processes involved under the two hypothesis. Recall that the clutter is a zero-mean random field and the target reflectivity function is a random field with the mean $\overline{T}(\boldsymbol{y})$ and autocovariance function R^T. Note that the discriminant functional for a deterministic target model can be obtained by simply setting the second-order statistics of the target reflectivity function to zero. The assumption of random reflectivity is justified for a distributed aperture array as the scattering properties of a typical target vary with the angle of incidence and scattering.

Using (15), (20), (25), (26) and (29), we obtain

$$\mathrm{E}[\mathbf{m}|\mathcal{H}_0] = \mathbf{0} \tag{30}$$

$$\mathrm{Cov}[\mathbf{m}|\mathcal{H}_0] = \mathbf{R}_\mathbf{n} =: \mathbf{R}_0 \tag{31}$$

$$\mathrm{E}[\mathbf{m}|\mathcal{H}_1] = \mathbf{G}_y \mathrm{E}[\mathbf{m}_\mathbf{r}|\mathcal{H}_1] = \mathbf{G}_y \overline{\mathbf{m}}_\mathbf{r} \tag{32}$$

$$\mathrm{Cov}[\mathbf{m}|\mathcal{H}_1] = \mathbf{G}_y(\mathbf{R}_T + \mathbf{R}_\mathbf{n})\mathbf{G}_y^H + \mathbf{R}_\mathbf{n} =: \mathbf{R}_1 \tag{33}$$

where $\overline{\mathbf{m}}_\mathbf{r}$ denotes $\mathrm{E}[\mathbf{m}_\mathbf{r}|\mathcal{H}_1]$ and $\mathbf{G}_y^H$ denotes the Hermitian transpose of $\mathbf{G}_y$. Using (14) and (17), for statistical targets, each component of $\overline{\mathbf{m}}_\mathbf{r}$ is

$$\mathrm{E}[\hat{m}_j(\omega)|\mathcal{H}_1] = \overline{\hat{m}}_j(\omega) \simeq -\mathcal{G}_{y,j}\overline{T}(\boldsymbol{y})\omega^2 \bar{\hat{E}}^{\mathrm{in}}(\boldsymbol{y}, \omega) \tag{34}$$

where $\overline{T}$ and $\bar{\hat{E}}^{\mathrm{in}}$ are the mean value of the target T and the incident field $\hat{E}^{\mathrm{in}}$, respectively.

$\mathbf{R}_T$ in (33) denotes the autocovariance of the noise- and clutter-free reference measurements in the presence of a statistical target, which is given by[1]

$$\mathbf{R}_T(\omega, \omega') = \mathrm{E}\left[\left(\mathbf{m}_\mathbf{r}^{(0)}(\omega) - \overline{\hat{\mathbf{m}}}_\mathbf{r}(\omega)\right)\left(\mathbf{m}_\mathbf{r}^{(0)}(\omega') - \overline{\hat{\mathbf{m}}}_\mathbf{r}(\omega')\right)^H\right] \tag{35}$$

where $\mathbf{m}_\mathbf{r}^{(0)} = \left[\hat{m}_j^{(0)}, \hat{m}_j^{(0)}, \ldots, \hat{m}_j^{(0)}\right]^T$ is the vector of the noise- and clutter-free reference measurements.

$\mathbf{R}_\mathbf{n}$ in (33) and (33) is the autocovariance of the measurements due to clutter and noise, i.e.

$$\mathbf{R}_\mathbf{n}(\omega, \omega') = \mathrm{E}[\mathbf{n}(\omega)\mathbf{n}^H(\omega')]. \tag{36}$$

We wish to determine a linear discriminant functional which maximizes the SNR of the output of the discriminant functional, which we call the *test statistic*, and denote it with λ. The linear discriminant functional involved in our problem has the form

$$\lambda = \langle \mathbf{m}, \mathbf{w} \rangle := \int \mathbf{w}^H \mathbf{m}\, \mathrm{d}\omega = \sum_{i, i \neq j} \int w_i^*(\omega)\hat{m}_i^j(\omega)\, \mathrm{d}\omega \tag{37}$$

where $\mathbf{w}$ is a template given by

$$\mathbf{w} = [w_1 \quad w_2 \quad \cdots \quad w_N]^T. \tag{38}$$

(37) is a general form for the linear discriminant functional and can be applied to both single and multiple frequency measurements. For single frequency measurements, the integral can simply be omitted.

The expression for the SNR of λ for processes with finite first- and second-order statistics is given as [34, 43]

$$\mathrm{SNR}_\lambda = \frac{|\mathrm{E}[\lambda|\mathcal{H}_1] - \mathrm{E}[\lambda|\mathcal{H}_0]|}{\sqrt{1/2(\mathrm{Var}[\lambda|\mathcal{H}_1] + \mathrm{Var}[\lambda|\mathcal{H}_0])}}. \tag{39}$$

[3] Note that $\mathbf{R}_T(\omega, \omega')$ can be obtained from *a priori* statistical target information where $\mathrm{E}[\hat{\mathbf{m}}_j^{(0)}(\omega)\hat{\mathbf{m}}_j^{*(0)}(\omega)] \simeq \int\int g(\mathbf{x}_j, \boldsymbol{y}, \omega)g^*(\mathbf{x}_j, \boldsymbol{y}', \omega')\mathrm{E}[T(\boldsymbol{y})T^*(\boldsymbol{y}')]\omega^2\omega'^2\mathrm{E}[\hat{E}^{\mathrm{in}}(\boldsymbol{y}, \omega)\hat{E}^{\mathrm{in}^*}(\boldsymbol{y}', \omega')]\, \mathrm{d}\boldsymbol{y}\, \mathrm{d}\boldsymbol{y}'$.

Each term in (39) can be determined using (30)–(33). The numerator is given by

$$\mathrm{E}[\lambda|\mathcal{H}_1] - \mathrm{E}[\lambda|\mathcal{H}_0] = \langle \mathbf{G}_y \overline{\mathbf{m}}_\mathbf{r}, \mathbf{w} \rangle. \tag{40}$$

The variance of λ can be expressed as

$$\mathrm{Var}[\lambda|\mathcal{H}_k] = \mathrm{E}[|\langle \mathbf{m}, \mathbf{w} \rangle|^2 |\mathcal{H}_k], \qquad k = 0, 1, \tag{41}$$

$$= \int \mathbf{w}^H \mathbf{R}_k \mathbf{w} \, \mathrm{d}\omega \, \mathrm{d}\omega' \tag{42}$$

$$=: \langle \mathcal{R}_k \mathbf{w}, \mathbf{w} \rangle, \qquad k = 0, 1, \tag{43}$$

where $\mathcal{R}_k$, $k = 0, 1$, is a symmetric non-negative definite integral operator with the matrix kernel $\mathbf{R}_k$. Note that the integration in (41) should be understood to be elementwise. Plugging (41) into (39), we obtain

$$\mathrm{Var}[\lambda|\mathcal{H}_1] + \mathrm{Var}[\lambda|\mathcal{H}_0] = \int \mathbf{w}^H \left[\mathbf{R}_1 + \mathbf{R}_0\right] \mathbf{w} \, \mathrm{d}\omega \, \mathrm{d}\omega' \tag{44}$$

$$= \int \mathbf{w}^H \underbrace{\left[\mathbf{G}_y (\mathbf{R}_T + \mathbf{R}_\mathbf{n}) \mathbf{G}_y^H + 2\mathbf{R}_\mathbf{n}\right]}_{2\overline{\mathbf{R}}} \mathbf{w} \, \mathrm{d}\omega \, \mathrm{d}\omega' \tag{45}$$

$$=: \langle 2\overline{\mathcal{R}} \mathbf{w}, \mathbf{w} \rangle \tag{46}$$

where $\overline{\mathcal{R}}$ is a symmetric, non-negative definite operator with the matrix kernel $\overline{\mathbf{R}}$. Using (39), (40) and (44), the SNR_λ^2 can be expressed in terms of the unknown template as follows:

$$J(\mathbf{w}) = \mathrm{SNR}_\lambda^2 = \frac{|\langle \mathbf{G}_y \overline{\mathbf{m}}_\mathbf{r}, \mathbf{w} \rangle|^2}{1/2 \langle (\mathcal{R}_1 + \mathcal{R}_0)\mathbf{w}, \mathbf{w} \rangle}. \tag{47}$$

The optimal linear template maximizing $J(\mathbf{w})$ is then

$$\mathbf{w}_{\mathrm{opt}} = \overline{\mathcal{R}}^{-1} \mathbf{G}_y \overline{\mathbf{m}}_\mathbf{r}. \tag{48}$$

Equation (48) shows that the optimal template is location dependent. A detailed derivation of the optimal linear template can be found in appendix A.

Note that for deterministic targets, the optimal template can be obtained from the one derived for statistical targets by simply setting $\mathbf{R}_T = 0$. For deterministic targets, further simplifications can be obtained when the measurements due to clutter and noise are wide-sense stationary and uncorrelated. In this case, $\mathbf{R}_\mathbf{n}$ reduces to a diagonal matrix. Without loss of generality, if the first receiver is the reference, then

$$R_n^{ii}(\omega, \omega') = S_n^{i+1}(\omega) \delta(\omega - \omega'), \qquad i = 1, \ldots, N-1, \tag{49}$$

where $S_n^i(\omega)$ is the power spectral density function of the measurements at the ith receiver due to clutter and noise. From (45) and (27), the kernel of $\overline{\mathcal{R}}$ also reduces to a diagonal matrix. We define

$$\overline{\mathbf{S}}(\omega) = \int \overline{\mathbf{R}}(\omega, \omega') \, \mathrm{d}\omega'. \tag{50}$$

Thus, under the deterministic target and wide-sense stationarity assumptions, (48) becomes

$$\mathbf{w}_{\mathrm{opt}} = \overline{\mathbf{S}}^{-1}(\omega) \mathbf{G}_y(\omega) \overline{\mathbf{m}}_\mathbf{r}(\omega) \tag{51}$$

where $\overline{\mathbf{S}}$ is a diagonal matrix with elements $\overline{S}_i(\omega)$, $i = 1, \ldots, N$ and $i \neq j$, which is a function of $S_n^i(\omega)$ and the kernel of $\mathbf{G}_y$.

Note that one can form a different vectorized measurement model and obtain a different template and a test statistic λ_j for each reference measurement $\hat{m}_j$, $j = 1, \ldots, N$. The final image can be formed by the coherent sum of all the spatially resolved test statistics λ_j, $j = 1, \ldots, N$.

5. Optimal template examples for the free-space and a multi-pathing environment model

In this section, we focus on two specific examples of Green's function, namely the free-space and shoot-and-bounce models, and describe the optimal templates for passive image formation for a point target model.

In many applications, the target model can be simplified to a point scatterer, i.e.

$$T(\boldsymbol{y}) = T\delta(\boldsymbol{y} - \boldsymbol{y}_0). \tag{52}$$

Thus, the forward-propagation operator in (17) reduces to $\hat{g}(\mathbf{x}_i, \boldsymbol{y}_0, \omega)$ and its inverse becomes $1/\hat{g}(\mathbf{x}_i, \boldsymbol{y}_0, \omega)$ for some range of ω. For a moving target, (21) simplifies to

$$\hat{m}_i^j(\omega) = \frac{\hat{g}(\mathbf{x}_i, \boldsymbol{y}_0, \omega)}{\hat{g}(\mathbf{x}_j, \boldsymbol{y}_0, \omega)} \hat{m}_j(\omega) + \hat{\tilde{n}}_i(\omega). \tag{53}$$

Note that if $\hat{g}(\mathbf{x}_j, \boldsymbol{y}_0, \omega)$ has zeros in the range of frequencies considered, it can be replaced by its pseudo-inverse given in (19).

5.1. *Passive imaging in free-space*

The 3D free-space Green's function is given by

$$\hat{g}_0(\mathbf{x}, \mathbf{y}, \omega) = \frac{\mathrm{e}^{-\mathrm{i}k\|\mathbf{x}-\mathbf{y}\|}}{4\pi\|\mathbf{x} - \mathbf{y}\|} \tag{54}$$

where $k = \omega/c$ is the wavenumber and c denotes the speed of wave propagation in free-space. The above equation indicates that in free-space, the Green's function is a delay operator with a geometric spreading factor $\|\mathbf{x} - \mathbf{y}\|$. Under the point target assumption, the measurement at the ith receiver can be expressed in terms of the measurement at the jth receiver as follows:

$$\hat{m}_i^j(\omega) = \frac{\|\mathbf{x}_j - \mathbf{y}_0\|}{\|\mathbf{x}_i - \mathbf{y}_0\|} \mathrm{e}^{-\mathrm{i}k(\|\mathbf{x}_i - \mathbf{y}_0\| - \|\mathbf{x}_j - \mathbf{y}_0\|)} \hat{m}_j(\omega) + \hat{\tilde{n}}_i(\omega) \tag{55}$$

where $\mathbf{y}_0 = (\boldsymbol{y}_0, h(\boldsymbol{y}_0))$.

For a single pair of receivers, the point target approximation simplifies the detection template so that the matrix $\mathbf{G}_{\boldsymbol{y}}$ consists of diagonal elements, $\hat{g}(\mathbf{x}_i, \boldsymbol{y}, \omega)/\hat{g}(\mathbf{x}_j, \boldsymbol{y}, \omega)$.

Under the wide-sense stationary clutter assumption, and for the deterministic point target, it is straightforward to show that the diagonal elements $\overline{S}_i(\omega)$ of $\overline{\mathbf{S}}$ are given by

$$\overline{S}_i(\omega) = \left(\frac{1}{2}\frac{\|\mathbf{x}_j - \mathbf{y}\|^2}{\|\mathbf{x}_i - \mathbf{y}\|^2} + 1\right) S_n^i(\omega). \tag{56}$$

Each component of the optimal template is then given by

$$w_i = \left(\left(\frac{1}{2}\frac{\|\mathbf{x}_j - \mathbf{y}\|^2}{\|\mathbf{x}_i - \mathbf{y}\|^2} + 1\right) S_n^i(\omega)\right)^{-1} \frac{\|\mathbf{x}_j - \mathbf{y}\|}{\|\mathbf{x}_i - \mathbf{y}\|} \mathrm{e}^{-\mathrm{i}k(\|\mathbf{x}_i - \mathbf{y}\| - \|\mathbf{x}_j - \mathbf{y}\|)} \mathrm{E}[\hat{m}_j(\omega)] \tag{57}$$

where $i = 1, \ldots, N$ and $i \neq j$.

The first term in (57) is a filter which involves scaling due to geometric spreading factors and prewhitening due to colored noise and clutter measurements. Thus, the output of the linear discriminant functional can be viewed as a summation of correlations between the delayed, scaled and filtered replica of the reference measurement $\hat{m}_j$ and the measurement $\hat{m}_i$, $i \neq j$,

which is given by

$$\lambda(\mathbf{y}) = \sum_{i,i\neq j} \int \frac{\|\mathbf{x}_j - \mathbf{y}\|}{\|\mathbf{x}_i - \mathbf{y}\|} E^*[m_j'(\tau - (\|\mathbf{x}_i - \mathbf{y}\| - \|\mathbf{x}_j - \mathbf{y}\|)/c)]m_i(\tau)\,\mathrm{d}\tau \tag{58}$$

where $m_j'(\tau)$ is the filtered version of $m_j(\tau)$ where the filtering is as described in (57).

5.2. *Passive imaging in multiple-scattering environments*

For high frequencies, the Green's function of a smoothly varying background $c_b(\mathbf{x})$ can be approximated by the ray-theoretic Green's function [44]

$$\hat{g}(\mathbf{x}, \mathbf{y}, \omega) \simeq a(\mathbf{x}, \mathbf{y})\, \mathrm{e}^{-\mathrm{i}\omega\tau(\mathbf{x},\mathbf{y})} \tag{59}$$

where τ denotes the travel time from $\mathbf{x}$ to $\mathbf{y}$ and $a(\mathbf{x}, \mathbf{y})$ is the corresponding ray-theoretic amplitude that is derived by solving the eikonal and the (first) transport equations. This model can be iteratively updated by considering point scatterers embedded in smoothly varying background and Born series [45, 46].

A more useful approximation to Green's function can be obtained from the Foldy–Lax and T-matrix equations [47, 48]. Assuming that there are L point scatterers located at $\mathbf{y}_l$, $l = 1, \ldots, L$, together with the assumption that the scattered field from an individual point scatter is proportional to the free-space Green's function, $\hat{g}_0$, the scattered field from L scatterers is given by

$$\hat{E}^{\mathrm{sc}}(\mathbf{x}, \omega) = \sum_{l=1}^{L} \hat{g}_0(\mathbf{x}, \mathbf{y}_l, \omega) a_l \hat{E}_l(\mathbf{y}_l, \omega) \tag{60}$$

$$\hat{E}_l(\mathbf{y}_l, \omega) = \hat{E}^{\mathrm{in}}(\mathbf{y}_l, \omega) + \sum_{p,p\neq l} \hat{g}_0(\mathbf{y}_l, \mathbf{y}_p, \omega) a_p \hat{E}_p(\mathbf{y}_p, \omega). \tag{61}$$

Equation (60) says that the scattered field is the sum of the fields scattered from each scatterer; moreover, the field scattered from the lth scatterer is proportional to the field $\hat{E}_l$ that is incident upon the lth scatterer. (61) says that the lth local incident field is the overall incident field plus the field scattered from all other scatterers. If the scattering strength a_l, and the positions $\mathbf{y}_l$, $l = 1, \ldots, L$ are known, (61) can be solved for the $\hat{E}_l$; then the total field $\hat{E} = \hat{E}^{\mathrm{in}} + \hat{E}^{\mathrm{sc}}$ can be found from (60).

When the scatterers are well separated, the background Green's function can be written in the form

$$\hat{g}(\mathbf{x}, \mathbf{y}, \omega) = \sum_{s\in\text{paths}} \tilde{a}_s(\mathbf{x}, \mathbf{y}, \omega)\, \mathrm{e}^{-\mathrm{i}\omega\tau_s(\mathbf{x},\mathbf{y})} \tag{62}$$

where τ_s denotes the travel time along the path s and $\tilde{a}_s$ is an amplitude factor that depends on geometric spreading factors, and the strength of the scatterers a_l.

An approximation to (62) can be obtained by considering only the paths originating from the target to a background scatterer and from the background scatterer to the receiver. This results in L multi-path bounces between the target and background medium for L scatterers embedded in a homogenous medium. In this case, the Green's function of the background can be approximated by

$$\hat{g}(\mathbf{x}, \mathbf{y}, \omega) = \frac{\mathrm{e}^{-\mathrm{i}k\|\mathbf{x}-\mathbf{y}\|}}{4\pi\|\mathbf{x} - \mathbf{y}\|} + \sum_{l=1}^{L} a_l \frac{\mathrm{e}^{-\mathrm{i}k(\|\mathbf{y}_l-\mathbf{y}\|+\|\mathbf{x}-\mathbf{y}_l\|)}}{4\pi\|\mathbf{y}_l - \mathbf{y}\|\|\mathbf{x} - \mathbf{y}_l\|} \tag{63}$$

where $\mathbf{y}_l$ for $l = 1, \ldots, L$ denotes the location of the scatterers and a_l are the corresponding attenuation coefficients. The Green's function above is referred to as the shoot-and-bounce model.

The passive measurement model then becomes

$$\hat{m}_i^j(\omega) = H_j(\omega)\left[\alpha_0\beta_0\,\mathrm{e}^{-\mathrm{i}kr^{ij}} + \sum_{l=1}^{L}\left(a_l\beta_l\alpha_0\,\mathrm{e}^{-\mathrm{i}kr_l^{ij}} + a_l\beta_l\alpha_0\,\mathrm{e}^{-\mathrm{i}k\bar{r}_l^{ij}}\right) + \sum_{l,p=1}^{L} a_l a_p\beta_l\alpha_p\,\mathrm{e}^{-\mathrm{i}k\bar{r}_{lp}^{ij}}\right]\hat{m}_j(\omega) + \hat{\tilde{n}}_i(\omega) \tag{64}$$

where

$$H_j(\omega) = \left[\alpha_0^2 + \sum_{l=1}^{L}\left(a_l^2\alpha_l^2 + 2a_l\alpha_0\alpha_l\cos k\bar{r}_l^{jj}\right) + 2\sum_{l\neq p}^{L} a_l a_p\alpha_l\alpha_p\cos k\bar{r}_{lp}^{jj}\right]^{-1}, \tag{65}$$

$$r^{ij} = \|\mathbf{x}_i - \mathbf{y}_0\| - \|\mathbf{x}_j - \mathbf{y}_0\|, \tag{66}$$

$$r_l^{ij} = \|\mathbf{x}_i - \mathbf{y}_l\| + \|\mathbf{y}_l - \mathbf{y}_0\| - \|\mathbf{x}_j - \mathbf{y}_0\|, \tag{67}$$

$$\bar{r}_l^{ij} = \|\mathbf{x}_i - \mathbf{y}_0\| - \|\mathbf{x}_j - \mathbf{y}_l\| - \|\mathbf{y}_l - \mathbf{y}_0\|, \tag{68}$$

$$\bar{r}_{lp}^{ij} = \|\mathbf{x}_i - \mathbf{y}_l\| + \|\mathbf{y}_l - \mathbf{y}_0\| - \|\mathbf{x}_j - \mathbf{y}_p\| - \|\mathbf{y}_p - \mathbf{y}_0\|, \tag{69}$$

$a_{l(p)}$ is the attenuation coefficient of the lth (or pth) multi-path bounce, $\alpha_0 = 1/4\pi\|\mathbf{x}_j - \mathbf{y}_0\|$ and $\beta_0 = 1/4\pi\|\mathbf{x}_i - \mathbf{y}_0\|$, which correspond to the geometrical spreading factors of the direct-path propagation with respect to the jth and ith element, respectively, and $\alpha_{l(p)} = 1/4\pi\|\mathbf{x}_j - \mathbf{y}_{l(p)}\|\|\mathbf{y}_{l(p)} - \mathbf{y}_0\|$ and $\beta_l = 1/4\pi\|\mathbf{x}_i - \mathbf{y}_l\|\|\mathbf{y}_l - \mathbf{y}_0\|$, which represent the geometric spreading factors corresponding to multi-path propagation.

As shown in (66)–(69), r^{ij} corresponds to the range difference between the two direct-path measurements at the ith and jth elements; r_l^{ij} and $\bar{r}_l^{ij}$ correspond to the range differences between the lth multi-path measurement at the ith element and the direct path delay measurement at the jth element and vice versa; $\bar{r}_{lp}^{ij}$ corresponds to the range differences between the two multi-path measurements at the ith and jth elements. The $H_j(\omega)$ can be viewed as a deconvolution filter. The above equation shows that the measurement at the ith element is modeled as a sum of the appropriately delayed and filtered versions of the reference measurement $\hat{m}_j$.

Using the passive measurement model for a multi-path propagation medium given in (64) and the wide-sense stationary clutter model, each element of the optimal template becomes

$$w_i = \left(\left(\frac{1}{2}|D_{ij}(\omega)|^2 + 1\right)S_n^i(\omega)\right)^{-1} D_{ij}(\omega)\mathrm{E}[\hat{m}_j(\omega)] \tag{70}$$

where

$$D_{ij}(\omega) = H_j(\omega)\left[\alpha_0\beta_0\,\mathrm{e}^{-\mathrm{i}k\,r^{ij}} + \sum_{l=1}^{L}\left(a_l\beta_l\alpha_0\,\mathrm{e}^{-\mathrm{i}k\,r_l^{ij}} + a_l\beta_0\alpha_l\,\mathrm{e}^{-\mathrm{i}k\,\bar{r}_l^{ij}}\right) + \sum_{l,p=1}^{L} a_l a_p\beta_l\alpha_p\,\mathrm{e}^{-\mathrm{i}k\,\bar{r}_{lp}^{ij}}\right]. \tag{71}$$

The template in (70) and (71) shows that the resulting test-statistic value is the sum of the correlations between appropriately delayed and filtered reference measurement, m_j, and the measurement m_i. The delays in each term in (71) are as described in (64).

6. Resolution analysis

We focus our analysis on the deterministic point target model given by

$$T(\mathbf{y}) = T\delta(\mathbf{y} - \mathbf{y}_0) \tag{72}$$

and analyze how point targets are resolved in the image $\lambda(\mathbf{y})$. We analyze the resolution in terms of the PSF and the SNR of the spatially resolved test-statistic image for both free-space and multi-path propagation models described in the previous section.

The PSF, $K(\mathbf{y}, \mathbf{y}_0)$, of an imaging operator is defined as the image of a point object represented by the Dirac-delta function, $\delta(\mathbf{y} - \mathbf{y}_0)$, with $\mathbf{y}$ serving as the spatial index of the image and $\mathbf{y}_0$ as the location of the point target in the scene [38]. Since the test statistic is a random variable, the expected value of the spatially varying test statistic for a point target can be interpreted as the PSF, i.e.

$$K(\mathbf{y}, \mathbf{y}_0) := \mathrm{E}[\lambda(\mathbf{y})] \tag{73}$$

$$= \langle \mathrm{E}[\mathbf{m}],\ \overline{\mathcal{R}}^{-1}\mathbf{G}_y\overline{\mathbf{m}}_\mathbf{r}\rangle. \tag{74}$$

Note that for a deterministic point target model given by (72)

$$\mathrm{E}[\hat{m}_j(\omega)] = -\hat{g}(\mathbf{x}_j, \mathbf{y}_0, \omega)T\omega^2\bar{\hat{E}}^{\mathrm{in}}(\mathbf{y}_0, \omega) \tag{75}$$

with

$$\hat{E}^{\mathrm{in}}(\mathbf{y}_0, \omega) = \sum_{q=1}^{M} \hat{g}(\mathbf{y}_0, \mathbf{z}_q, \omega)\hat{p}_q(\omega) \tag{76}$$

where $\bar{\hat{E}}^{\mathrm{in}}$ is the mean value of the incident field $\hat{E}^{\mathrm{in}}$, p_q is the transmitted waveform from the qth transmitter located at $\mathbf{z}_q$, $q = 1, \ldots, M$, and M is the number of transmitters illuminating the scene.

The SNR of $\lambda(\mathbf{y})$ as defined in (39) can be interpreted as the *contrast-to-noise ratio* of the resulting image [38].

Without loss of generality, we first assume that there is a single pair of receivers and a single transmitter present in the scene. This allows us to simplify the analysis and distill the important aspects that can readily be generalized. We next extend our results to the case where there are multiple pairs of receivers and multiple transmitters.

6.1. Resolution analysis for the free-space model

6.1.1. PSF and SNR for two receivers and a single transmitter. We assume that there are two receivers located at $\mathbf{x}_1$ and $\mathbf{x}_2$, and a single transmitter located at $\mathbf{z}_1$ illuminating the scene. Thus, from (37), (54)–(57), the expression for the mean value of the spatially varying test statistic is

$$K(\mathbf{y}, \mathbf{y}_0) = \mathrm{E}[\lambda(\mathbf{y})] = \beta \int \overline{S}_2^{-1}(\omega)\omega^4\, \mathrm{e}^{-\mathrm{i}kr_{21}(\mathbf{y},\mathbf{y}_0)}\, |\hat{p}_1(\omega)|^2\, \mathrm{d}\omega \tag{77}$$

where

$$r_{21}^h(\mathbf{y}, \mathbf{y}_0) = \|\mathbf{x}_2 - \mathbf{y}\| - \|\mathbf{x}_1 - \mathbf{y}\| + \|\mathbf{x}_1 - \mathbf{y}_0\| - \|\mathbf{x}_2 - \mathbf{y}_0\| \tag{78}$$

$$\beta = \frac{T^2\|\mathbf{x}_1 - \mathbf{y}\|}{(4\pi)^4\|\mathbf{x}_2 - \mathbf{y}\|\|\mathbf{x}_1 - \mathbf{y}_0\|\|\mathbf{x}_2 - \mathbf{y}_0\|\|\mathbf{y}_0 - \mathbf{z}_0\|^2} \tag{79}$$

and $\overline{S}_2(\omega)$ is given by (56) for $i = 2$, $j = 1$; p_1 is the transmitted waveform. (77) defines the correlation of $\left|\overline{S}_2^{-1/2}(\omega)\omega^2\hat{p}_1(\omega)\right|$ with itself in the time domain. Clearly, the correlation peaks when $r_{12}(\mathbf{y}, \mathbf{y}_0) = 0$. In other words, for a point target located at $\mathbf{y}_0$, the peak correlation

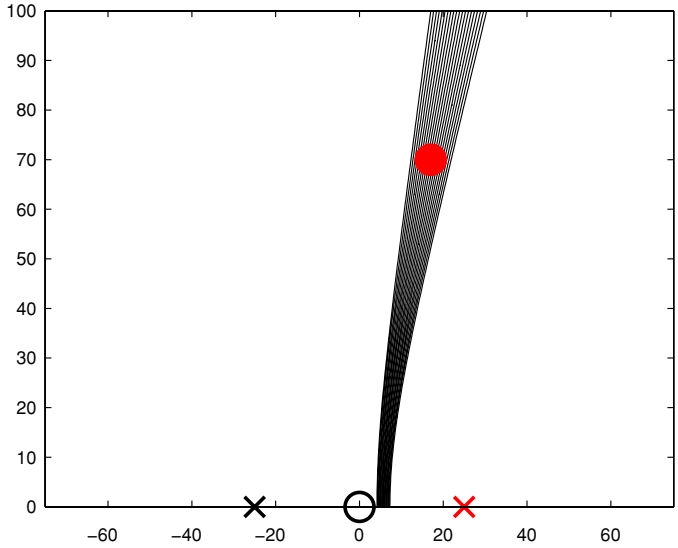

Figure 4. Hyperbolic isorange contours associated with a single transmitter and two receivers in free-space. The blank circle shows the transmitter location and the cross shows receiver locations. The solid circle shows the target location.

value occurs wherever

$$\|\mathbf{x}_2 - \mathbf{y}\| - \|\mathbf{x}_1 - \mathbf{y}\| = \|\mathbf{x}_2 - \mathbf{y}_0\| - \|\mathbf{x}_1 - \mathbf{y}_0\|. \tag{80}$$

(80) specifies a hyperbola on the plane defined by $h(\boldsymbol{y}) = h$ with foci located at $\boldsymbol{x}_1$ and $\boldsymbol{x}_2$. Thus, the test statistic due to a point target located at $\mathbf{y}_0$ is constant along this hyperbola. We shall refer to these hyperbolas along which the test-statistic values are constant as *hyperbolic isorange* contours. These isorange contours are illustrated in figure 4.

Note that if the measurements due to noise and clutter are white, under the narrowband assumption, (77) defines the auto-ambiguity function of the transmitted waveform p_1 [49, 50]. When the measurements due to noise and clutter are colored, (77) can be interpreted as a generalized auto-ambiguity function in which the contributions of the transmitted pulse at every frequency to the classical auto-ambiguity function is downweighted with the power of the noise and clutter measurements. The shape of this generalized auto-ambiguity function determines the intensity of the hyperbolas in the test statistics as shown by (77). More specifically, the support of the generalized auto-ambiguity function determines the set of hyperbolic paths that contribute to the width of the spread along the hyperbolas in the test-statistic image. In other words, delay due to r_{12}^h identifies the position in the auto-ambiguity function of $\left|\overline{S}_2^{-1/2}(\omega)\omega^2\hat{p}_1(\omega)\right|$ and selects the nearby hyperbola associated with that delay and with the amplitude proportional to the amplitude of the generalized auto-ambiguity function at that delay. This, in turn, forms a collection of hyperbolas with amplitudes related to the auto-ambiguity function and thus results in a 'spreading' in the image along these hyperbolas. Figure 5 illustrates this spreading in the PSF. The figure on the left is an example of an auto-ambiguity function. The figure on the right shows the PSF due to this auto-ambiguity function. The spreading was shown limited to the dotted lines on the auto-ambiguity function plot. It is clear from figure 5 that the spreading along the hyperbolas also depends on the range. As the target $\mathbf{y}_0$ is further away from the receivers, the spreading increases. This is due to the fact

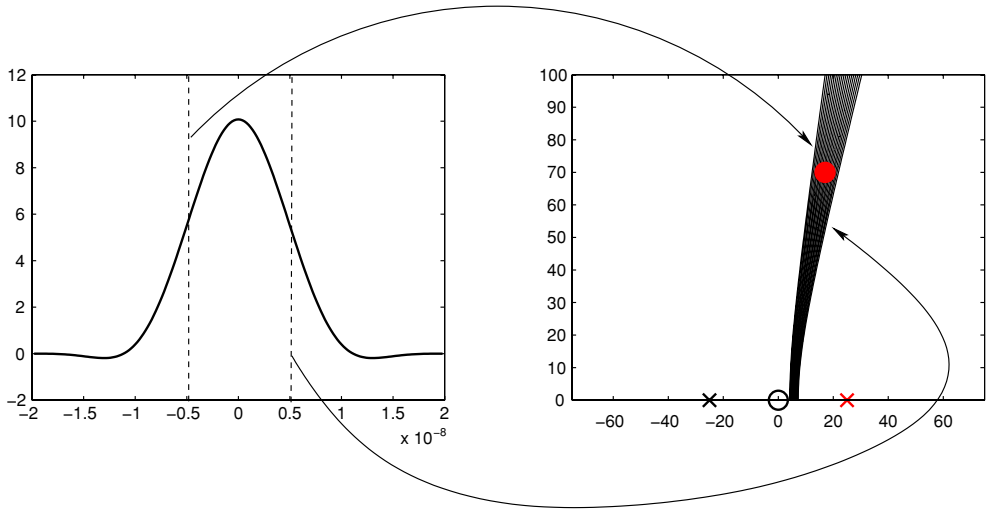

Figure 5. An illustration of the relationship between the auto-ambiguity function of the waveform (left) and the point spread function of the test-statistic image (right). The blank circle shows the transmitter location and the cross shows receiver locations. The solid circle shows the target location.

that the angular difference between $\mathbf{x}_1 - \mathbf{y}_0$ and $\mathbf{x}_2 - \mathbf{y}_0$ is smaller as the distance from $\mathbf{y}_0$ to the receivers becomes larger; therefore, nearby hyperbolic isorange curves deviate more from each other as $\mathbf{y}_0$ is further away from the receivers.

We performed a point target simulation to confirm our analysis. The simulation setup is as follows: there are two receivers located at $\mathbf{x}_1 = [36.6\ 0\ 6]^T$ and $\mathbf{x}_2 = [20\ 0\ 6]^T$, all in meters. The transmitter is located in the middle of the two receivers at $\mathbf{z}_1 = [28.3\ 0\ 6]^T$ m and the point target is located at $\mathbf{y}_0 = [45\ 70\ 0.3]^T$ m. The transmitted pulse, $p(t)$, is a 10 nanosecond (ns) continuous wave at 900 MHz. Figure 6 shows the resulting PSF. Note that the image of the point target is smeared along the hyperbolic path as the width widens with increasing range consistent with the above analysis. Additionally, since the test statistics have the same intensity along the hyperbolic isorange contours, one pair of receivers can only locate a target up to the isorange contour passing through the target location $\mathbf{y}_0$.

The SNR_λ^2 at each location of the image is given by

$$\mathrm{SNR}_\lambda^2 = \frac{T^2\|\mathbf{x}_1 - \mathbf{y}\|^2}{(4\pi)^4\|\mathbf{x}_1 - \mathbf{y}_0\|^2\|\mathbf{x}_2 - \mathbf{y}\|^2\|\mathbf{y}_0 - \mathbf{z}_1\|^2}\int \overline{S}_2^{-1}(\omega)\omega^4|\hat{p}_1(\omega)|^2\,\mathrm{d}\omega. \tag{81}$$

For the derivation of (81), see appendix B.2. We see from (81) that the SNR_λ^2 is directly related to the power of the transmitted waveform and inversely related to the power of measurements due to noise and clutter.

6.1.2. PSF and SNR for multiple receivers and multiple transmitters. The PSF of the imaging operator for $N \geqslant 2$ and for $M \geqslant 1$ is given by

$$K(\mathbf{y}, \mathbf{y}_0) = T^2\sum_{q=1}^{M}\sum_{i\neq j}^{N} C_1\int \overline{S}_i^{-1}(\omega)\omega^4\,\mathrm{e}^{-\mathrm{i}k\,r_{ij}^h(\mathbf{y},\mathbf{y}_0)}|\hat{p}_q(\omega)|^2\,\mathrm{d}\omega + T^2\sum_{q\neq q'}^{M}\sum_{i\neq j}^{N} C_2$$
$$\times\int \overline{S}_i^{-1}(\omega)\omega^4\,\mathrm{e}^{-\mathrm{i}k\,r_{ij}^h(\mathbf{y},\mathbf{y}_0)}\,\mathrm{e}^{-\mathrm{i}k(\|\mathbf{y}_0-\mathbf{z}_q\|-\|\mathbf{y}_0-\mathbf{z}_{q'}\|)}\,\hat{p}_q(\omega)\,\hat{p}_{q'}^*(\omega)\,\mathrm{d}\omega \tag{82}$$

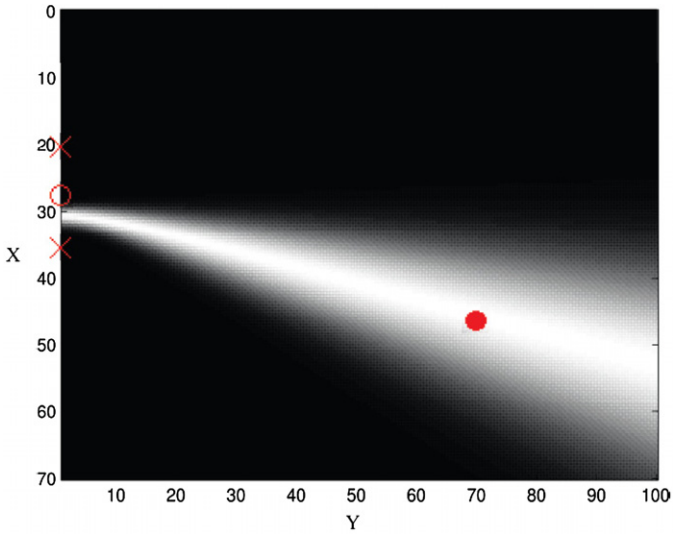

Figure 6. The PSF for the free-space propagation model resulting from using two receivers located at $[36.6\ 0\ 6]^T$ and $[20\ 0\ 6]^T$, and a single transmitter located at $[28.3\ 0\ 6]^T$. The blank circle shows the transmitter location and the cross shows receiver locations. The solid circle shows the target location.

where

$$r_{ij}^h(\mathbf{y}, \mathbf{y}_0) = \|\mathbf{x}_i - \mathbf{y}\| - \|\mathbf{x}_j - \mathbf{y}\| + \|\mathbf{x}_j - \mathbf{y}_0\| - \|\mathbf{x}_i - \mathbf{y}_0\|, \tag{83}$$

and C_1, C_2 are i, j, q, q' dependent scaling terms due to geometric spreading factors. (For a detailed derivation of (82) and the explicit forms of C_1 and C_2, see appendix B.1.)

Equation (82) shows that the PSF of the imaging operator is defined by the generalized auto-ambiguity and generalized cross-ambiguity functions of the transmitted waveforms p_q, $q = 1, \ldots, M$, where the generalized auto-ambiguity function is interpreted as discussed in the previous subsection. The first summation in (82) is due to the auto-ambiguity functions and the second summation is due to the cross-ambiguity functions of the transmitted waveforms.

Note that if there is a single transmitter illuminating the scene, i.e. $M = 1$, the second summation in (82) vanishes. Clearly for $M = 1$ and $N \geqslant 3$, there are multiple pairs of receivers generating multiple hyperbolic isorange contours, all intersecting at $\mathbf{y}_0$. The resulting image is the summation of these intersecting hyperbolas forming a bright spot at the location of the target, $\mathbf{y}_0$. Figure 7 illustrates the PSF of the image using three receivers and a single transmitter.

If there are multiple transmitters illuminating the scene, i.e. $M \geqslant 2$, (82) shows that the generalized cross-ambiguity functions of the transmitted waveforms have peaks occurring at

$$r_{ij}^h(\mathbf{y}, \mathbf{y}_0) = \|\mathbf{x}_i - \mathbf{y}\| - \|\mathbf{x}_j - \mathbf{y}\| + \|\mathbf{x}_j - \mathbf{y}_0\| - \|\mathbf{x}_i - \mathbf{y}_0\| \tag{84}$$

$$= \|\mathbf{y}_0 - \mathbf{z}_q\| - \|\mathbf{y}_0 - \mathbf{z}_{q'}\|. \tag{85}$$

(84) defines additional hyperbolas with the same foci, but different radii than the hyperbolas in the first summation. Clearly, for arbitrary transmitted waveforms, these hyperbolas do not intersect at the target location when $\mathbf{z}_q \neq \mathbf{z}_{q'}$ leading to artifacts in the image. These artifacts can be avoided if the transmitted waveforms have cross-ambiguity functions with a relatively low amplitude.

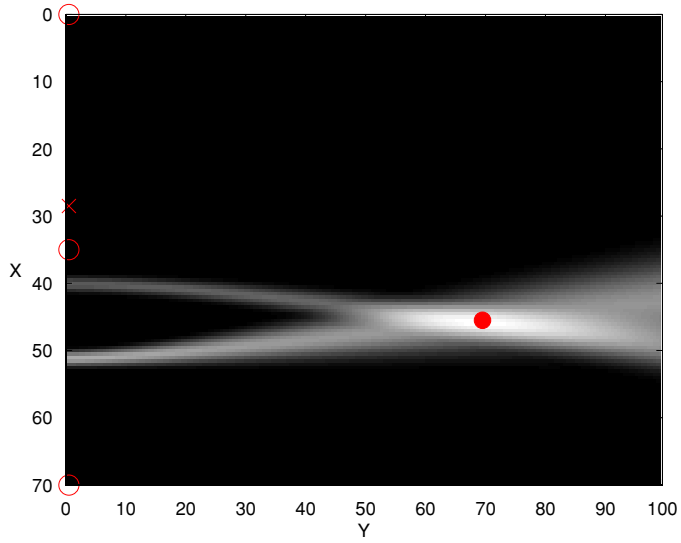

Figure 7. The PSF for the free-space propagation model resulting from using three receivers located at $[0\ \ 0\ \ 6]^T$, $[35\ \ 0\ \ 6]^T$ and $[70\ \ 0\ \ 6]^T$, and a single transmitter located at $[28.3\ \ 0\ \ 6]^T$. The intersection of the two hyperbolas, i.e. the bright spot indicated by a solid circle, shows the target location.

The impact of having more than two receivers and more than one transmitter can also be observed in the SNR of the image. The SNR_λ^2 is given by the following equation:

$$\mathrm{SNR}_\lambda^2 = T^2 \sum_{q=1}^{M} \sum_{i \neq j}^{N} C_1' \int \overline{S}_i^{-1}(\omega)\omega^4 |\hat{p}_q(\omega)|^2 \, \mathrm{d}\omega + T^2 \sum_{q \neq q'}^{M} \sum_{i \neq j}^{N} 2C_2' \, \mathrm{Re}\left[\int \overline{S}_i^{-1}(\omega)\omega^4 \, \mathrm{e}^{-\mathrm{i}k(\|\mathbf{y}_0 - \mathbf{z}_q\| - \|\mathbf{y}_0 - \mathbf{z}_{q'}'\|)} \hat{p}_q(\omega) \hat{p}_{q'}^*(\omega) \, \mathrm{d}\omega \right] \tag{86}$$

where C_1' and C_2' are i, j, q, q' dependent scaling terms due to geometric spreading factors. (See appendix B.2 for the definitions of these quantities and the derivation of (86).)

Note that the first summation in (86) is the SNR_λ^2 of the true target image, which results from the auto-ambiguity functions of the transmitted waveforms, while the second summation is the SNR_λ^2 of the artifact component in the image, which results from the cross-ambiguity functions of the transmitted waveforms.

Compared to the SNR_λ^2 of the two-receiver and a single-transmitter scenario given in (81), (86) shows that for each additional receiver, the SNR_λ^2 of the true target image increases by $T^2 C_1' \int \overline{S}_i^{-1}(\omega)\omega^4 |\hat{p}(\omega)|^2 \, \mathrm{d}\omega$. For M transmitters, the SNR_λ^2 of the true target image increases roughly by a factor of M. However, we see that the SNR_λ^2 of the artifact component also increases with the increasing number of transmitters with the worse case occurring when the same waveforms, i.e. $\hat{p}_q(\omega) = \hat{p}_{q'}(\omega)$ for all ω and $q \neq q'$, are transmitted from all transmitters.

6.2. Resolution analysis for a multi-path model

We consider the shoot-and-bounce multi-path Green's function model described in section 5 and further assume that all multi-path bounces are specular reflections. This allows

us to model the environment as a collection of mirror planes. Each plane is characterized by its normal vector **a**, and affine plane equation, $\mathcal{A}$ defined as

$$\mathcal{A} := \{\mathbf{v} : \mathbf{v} \cdot \mathbf{a} = \upsilon\} \tag{87}$$

where υ is a scalar that determines the location of the wall. This allows us to express the multi-path components of the Green's function given in section 5 using the *mirror* antenna element locations as follows:

$$\hat{g}(\mathbf{x}, \mathbf{y}, \omega) = \frac{\mathrm{e}^{-\mathrm{i}k\|\mathbf{x}-\mathbf{y}\|}}{4\pi\|\mathbf{x}-\mathbf{y}\|} + \sum_{l=1}^{L} a_l \frac{\mathrm{e}^{-\mathrm{i}k\|\mathbf{x}^l-\mathbf{y}\|}}{4\pi\|\mathbf{x}^l-\mathbf{y}\|} \tag{88}$$

$$= \sum_{l=0}^{L} a_l \frac{\mathrm{e}^{-\mathrm{i}k\|\mathbf{x}^l-\mathbf{y}\|}}{4\pi\|\mathbf{x}^l-\mathbf{y}\|}, \qquad a_0 = 1, \quad \mathbf{x}^0 = \mathbf{x} \tag{89}$$

where

$$\mathbf{x}^l = \mathbf{x} - 2\frac{\mathbf{x}\cdot\mathbf{a}_l - \upsilon}{\|\mathbf{a}_l\|^2}\mathbf{a}_l, \quad l = 1, \ldots, L, \tag{90}$$

is the reflection of **x** about the plane, $\mathcal{A}_l$ that is defined by the normal $\mathbf{a}_l$ associated with the lth ($l = 1, \ldots, L$) multi-path bounce and a_l is the corresponding attenuation coefficient.

The optimal linear template for the multi-path propagation model is given by

$$w_i = -\overline{S}_i^{-1}(\omega)\tilde{D}_{ij}(\omega)T\omega^2 \sum_{q=1}^{M}\sum_{p,\nu=0}^{L} \frac{a_p a_\nu \,\mathrm{e}^{-\mathrm{i}k(\|\mathbf{x}_j^p-\mathbf{y}_0\|+\|\mathbf{y}_0-\mathbf{z}_q^\nu\|)}}{(4\pi)^2\left\|\mathbf{x}_j^p-\mathbf{y}_0\right\|\left\|\mathbf{y}_0-\mathbf{z}_q^\nu\right\|}\hat{p}_q(\omega) \tag{91}$$

where

$$\overline{S}_i(\omega) = \left(\tfrac{1}{2}|\tilde{D}_{ij}(\omega)|^2 + 1\right)S_n^i(\omega) \tag{92}$$

with $S_n^i(\omega)$ being the power spectral density function of the measurement due to clutter and noise at the ith receiver;

$$\tilde{D}_{ij}(\omega) = \frac{\hat{g}(\mathbf{x}_i, \mathbf{y}, \omega)}{\hat{g}(\mathbf{x}_j, \mathbf{y}, \omega)}$$

$$= \tilde{H}_j(\omega)\sum_{l,p=0}^{L} a_l a_p \frac{\mathrm{e}^{-\mathrm{i}k(\|\mathbf{x}_i^l-\mathbf{y}\|-\|\mathbf{x}_j^p-\mathbf{y}\|)}}{(4\pi)^2\left\|\mathbf{x}_i^l-\mathbf{y}\right\|\left\|\mathbf{x}_j^p-\mathbf{y}\right\|} \tag{93}$$

with

$$\tilde{H}_j(\omega) = \left(\sum_{p=0}^{L}\frac{a_p^2}{(4\pi)^2\left\|\mathbf{x}_j^p-\mathbf{y}\right\|^2} + \sum_{p\neq p'}^{L}\frac{2a_p a_{p'}\cos\frac{\omega}{c}\left(\left\|\mathbf{x}_j^p-\mathbf{y}\right\| - \left\|\mathbf{x}_j^{p'}-\mathbf{y}\right\|\right)}{(4\pi)^2\left\|\mathbf{x}_j^p-\mathbf{y}\right\|\left\|\mathbf{x}_j^{p'}-\mathbf{y}\right\|}\right)^{-1}. \tag{94}$$

a_l, a_p, a'_p in the above equations are the attenuation coefficients associated with the corresponding multi-path bounces. Note that $\mathbf{x}_i^0 = \mathbf{x}_i$, $\mathbf{x}_j^0 = \mathbf{x}_j$; and $\mathbf{x}_i^l$, $\mathbf{x}_j^p$, l, $p = 1, \ldots, L$, are the reflections of the receivers located at $\mathbf{x}_i$ and $\mathbf{x}_j$ about the planes $\mathcal{A}_l$ and $\mathcal{A}_p$, respectively. We refer to these receivers as *mirror receivers*. In (91), $\mathbf{z}_q^0 = \mathbf{z}_q$, $q = 1, \ldots, M$, denotes the location of the qth transmitter. $\mathbf{z}_q^\nu$, $\nu = 1, \ldots, L$, are the reflections of the transmitters located at $\mathbf{z}_q$ about the plane $\mathcal{A}_\nu$. We refer to these transmitters as *mirror transmitters*.

6.2.1. PSF and SNR for two receivers and a single transmitter. We assume that there are two receivers located at $\mathbf{x}_1$ and $\mathbf{x}_2$ and a single transmitter located at $\mathbf{z}_1$. In this scenario, we can show that the PSF of the imaging operator is given by

$$K(\mathbf{y},\mathbf{y}_0) = T^2 \sum_{l,l',p,p',\nu,\nu'=0}^{L} C \int \overline{S}_2^{-1}(\omega)\tilde{H}_1(\omega)\omega^4 \times \mathrm{e}^{-\mathrm{i}k\,[r_{21}^{hm}(\mathbf{y},\mathbf{y}_0;l,p;l',p')+(\|\mathbf{y}_0-\mathbf{z}_1^{\nu}\|-\|\mathbf{y}_0-\mathbf{z}_1^{\nu'}\|)]}|\hat{p}_1(\omega)|^2\,\mathrm{d}\omega \tag{95}$$

where

$$r_{21}^{hm}(\mathbf{y},\mathbf{y}_0;l,p,l',p') = \left\|\mathbf{x}_2^{l}-\mathbf{y}\right\| - \left\|\mathbf{x}_1^{p}-\mathbf{y}\right\| + \left\|\mathbf{x}_1^{p'}-\mathbf{y}_0\right\| - \left\|\mathbf{x}_2^{l'}-\mathbf{y}_0\right\| \tag{96}$$

and C is an l, l', p, p', ν, ν' dependent scaling term due to geometric spreading factors and multi-path attenuation coefficients. (For an explicit form of C and the derivation of (95), see appendix B.3.)

Similar to the free-space case, (95) can be interpreted as a generalized auto-ambiguity function of the transmitted waveform p_1 which attains its maximum whenever

$$r_{21}^{hm}(\mathbf{y},\mathbf{y}_0;l,p,l',p') + \left\|\mathbf{y}_0-\mathbf{z}_1^{\nu}\right\| - \left\|\mathbf{y}_0-\mathbf{z}_1^{\nu'}\right\| = 0. \tag{97}$$

Clearly, for all the points $\mathbf{y}$ on the intersection of the ground topography and the hyperboloid,

$$\left\|\mathbf{x}_2^{l}-\mathbf{y}\right\| - \left\|\mathbf{x}_1^{p}-\mathbf{y}\right\| = \left\|\mathbf{x}_2^{l'}-\mathbf{y}_0\right\| - \left\|\mathbf{x}_1^{p'}-\mathbf{y}_0\right\| + \left\|\mathbf{y}_0-\mathbf{z}_1^{\nu'}\right\| - \left\|\mathbf{y}_0-\mathbf{z}_1^{\nu}\right\|, \tag{98}$$

(97) becomes zero. Thus, (95) shows that the test-statistic image is the sum of hyperbolas with foci located at $\mathbf{x}_2^{l}$ and $\mathbf{x}_1^{p}$, $l, p = 0, \ldots, L$, corresponding to the locations of the real and mirror receivers. The hyperbolas corresponding to $l = l'$, $p = p'$ and $\nu = \nu'$ intersect at the correct target location and increase the test-statistic value at the correct target location by roughly a factor of $(L+1)^3$, where L being the number of multi-path bounces. However, the hyperbolas where $l \neq l'$, or $p \neq p'$, or $\nu \neq \nu'$ may peak at incorrect locations in the image resulting in artifacts.

Figure 8 illustrates the increase in the target detectability and artifacts due to multi-path bounces.

The SNR_λ^2 for this scenario is given by

$$\begin{aligned}\mathrm{SNR}_\lambda^2 = {} & T^2\left(C_1' + \sum_{l,p,\nu\neq 0}^{L} C_2'\right)\int \overline{S}_2^{-1}(\omega)|\tilde{H}_1(\omega)|^2\omega^4|\hat{p}_1(\omega)|^2\,\mathrm{d}\omega \\ & + T^2\sum_{\alpha\neq\alpha'}^{L} 2C_3'\,\mathrm{Re}\Bigg[\int \overline{S}_2^{-1}(\omega)|\tilde{H}_1(\omega)|^2\omega^4\,\mathrm{e}^{-\mathrm{i}k\,r_{21}^{hm}(\mathbf{y},\mathbf{y};l,p;l',p')} \\ & \times \mathrm{e}^{-\mathrm{i}k(\|\mathbf{x}_1^{p''}-\mathbf{y}_0\|-\|\mathbf{x}_1^{p'''}-\mathbf{y}_0\|+\|\mathbf{y}_0-\mathbf{z}_1^{\nu}\|-\|\mathbf{y}_0-\mathbf{z}_1^{\nu'}\|)}|\hat{p}_1(\omega)|^2\,\mathrm{d}\omega\Bigg]\end{aligned} \tag{99}$$

where $r_{21}^{hm}(\mathbf{y},\mathbf{y};l,p,l',p')$ is as defined in (96); α and α' are multi-indices defined by $\alpha = (l,p,p'',\nu)$, $p \neq p''$, $\alpha' = (l',p',p''',\nu')$, $p' \neq p'''$; and C_1, C_2, C_3 are α, α' dependent scaling terms due to geometric spreading factors and multi-path attenuation coefficients. (For the explicit definitions of C_1', C_2', C_3' and the derivation of (99), see appendix B.4 for $i = 2$, $j = 1$ and $q = 1$.)

Note that the first summation in (99) corresponds to the SNR_λ^2 of the true target image due to the direct-path propagation, the second summation in the SNR_λ^2 corresponds to the true target image due to the multi-path propagation and the third summation is the SNR_λ^2 of the artifacts in the image.

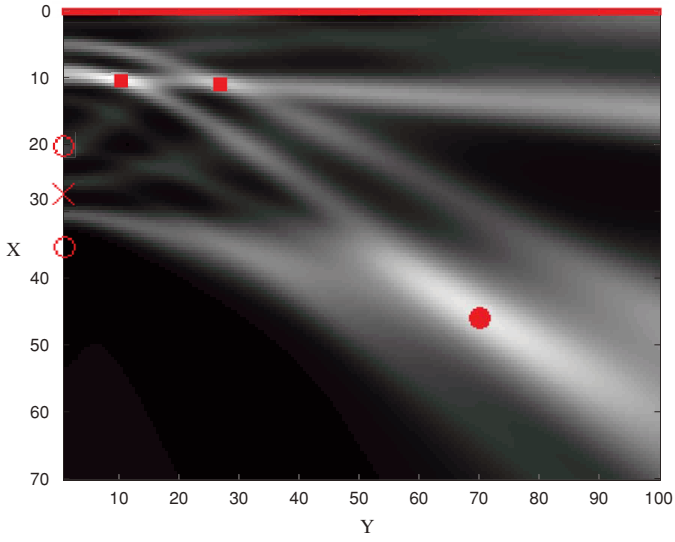

Figure 8. The PSF for the shoot-and-bounce multi-path propagation model. The shoot-and-bounce model includes a perfectly reflecting wall at $x = 0$. The bright spot, indicated by a solid circle, shows the target location and the two bright spots in the upper left corner, indicated by the solid squares, are the artifacts due to multi-path. The location of the transmitters and receivers and the transmitted pulse parameters are as described in figure 6.

As compared to (81), the SNR_λ^2 of the image obtained with two receivers and a single transmitter operating in free-space, the SNR_λ^2 of the true target image in a multi-path environment increases by roughly a factor of $(L+1)^3$, where L is the number of the multi-path bounces. However, there are also additional artifacts in the image in multi-path environments as shown by the third summation in (99). The number of summands in the third summation is roughly $[L(L+1)/2]^4$. Note that although the number of summands in the SNR_λ^2 of the artifact component is much larger than that of the true target image, their strength is relatively low, because the transmitted waveform is auto-correlated with a delayed version of itself, i.e. the energy of the transmitted waveforms are not coherently integrated, as indicated by the non-zero phase terms in the third summation of (99).

6.2.2. PSF and SNR for multiple receivers and multiple transmitters. The PSF of the test-statistic image for $N \geqslant 2$ and $M \geqslant 1$ is given by

$$\begin{aligned} K(\mathbf{y}, \mathbf{y}_0) = {} & T^2 \sum_{q=1}^{M} \sum_{i \neq j}^{N} \sum_{l,p,\nu=0}^{L} C_1 \int \overline{S}_i^{-1}(\omega) \tilde{H}_j(\omega) \omega^4 \, \mathrm{e}^{-\mathrm{i}k\, r_{ij}^{hm}(\mathbf{y},\mathbf{y}_0;l,p;l,p)} |\hat{p}_q(\omega)|^2 \, \mathrm{d}\omega \\ & + T^2 \sum_{q \neq q'}^{M} \sum_{i \neq j}^{N} \sum_{l \neq l', p \neq p', \nu \neq \nu'}^{L} C_2 \int \overline{S}_i^{-1}(\omega) \tilde{H}_j(\omega) \omega^4 \\ & \times \mathrm{e}^{-\mathrm{i}k\,[r_{ij}^{hm}(\mathbf{y},\mathbf{y}_0;l,p,l',p') + (\|\mathbf{y}_0 - \mathbf{z}_q^{\nu}\| - \|\mathbf{y}_0 - \mathbf{z}_{q'}^{\nu'}\|)]} \hat{p}_q(\omega) \hat{p}_{q'}^*(\omega) \, \mathrm{d}\omega \end{aligned} \tag{100}$$

where

$$r_{ij}^{hm}(\mathbf{y}, \mathbf{y}_0; l, p; l, p) = \left\|\mathbf{x}_i^l - \mathbf{y}\right\| - \left\|\mathbf{x}_j^p - \mathbf{y}\right\| + \left\|\mathbf{x}_j^p - \mathbf{y}_0\right\| - \left\|\mathbf{x}_i^l - \mathbf{y}_0\right\| \tag{101}$$

and C_1, C_2 are $q, q', i, j, l, p, \nu, l', p', \nu'$ dependent scaling terms due to geometrical spreading factors and multi-path attenuation coefficients. (For explicit definitions of C_1, and C_2 and the derivation of (100), see appendix B.3.)

Note that the first summation in (100) contributes to the reconstruction of the true target image, while the second summation contributes to the reconstruction of the artifact component in the image.

When there is only a single transmitter illuminating the scene, multiple hyperbolic isorange contours with foci at the real and mirror receiver locations intersect at the correct target location, $\mathbf{y}_0$, as indicated by the first term in (100). As a result the PSF of the imaging operator increases roughly by a factor of $(N-1)$ (the number of multi-path bounces) as compared to the two-receiver scenario described in (95). However, similar to the two-receiver and a single-transmitter scenario operating in multi-path environments, additional hyperbolic isorange contours with the same foci but different radii than the ones in the first summation in (100) contribute to the reconstructions of artifacts in the image.

For the multiple-transmitter scenario, the PSF at the correct target location increases roughly by a factor of M as compared to the PSF for the single-transmitter scenario in (100). However, (100) shows that unless the transmitted waveforms have good cross-ambiguity functions, such as pseudo-orthogonality, the cross-ambiguity terms due to the following hyperbolas,

$$r_{ij}^{hm}(\mathbf{y}, \mathbf{y}_0; l, p, l', p') = \left\|\mathbf{y}_0 - \mathbf{z}_{q'}^{v'}\right\| - \left\|\mathbf{y}_0 - \mathbf{z}_q^{v}\right\| \tag{102}$$

for $q \neq q'$ and $l \neq l'$, $p \neq p'$ or $v \neq v'$ may intersect at $\mathbf{y} \neq \mathbf{y}_0$, resulting in additional artifacts in the image.

The effect of having multiple receivers and transmitters in a multi-path environment can be also observed in the SNR_λ^2:

$$\begin{aligned}
\mathrm{SNR}_\lambda^2 = {} & T^2 \sum_{q=1}^{M} \sum_{i\neq j}^{N} C_1' \int \overline{S}_i^{-1}(\omega) |\tilde{H}_j(\omega)|^2 \omega^4 |\hat{p}_q(\omega)|^2 \,\mathrm{d}\omega \\
& + T^2 \sum_{q=1}^{M} \sum_{i\neq j}^{N} \sum_{l,p,v\neq 0}^{L} C_2' \int \overline{S}_i^{-1}(\omega) |\tilde{H}_j(\omega)|^2 \omega^4 |\hat{p}_q(\omega)|^2 \,\mathrm{d}\omega \\
& + T^2 \sum_{q\neq q'}^{M} \sum_{i\neq j}^{N} \sum_{\alpha\neq\alpha'}^{L} 2C_3' \,\mathrm{Re}\Bigg[\int \overline{S}_i^{-1}(\omega) |\tilde{H}_j(\omega)|^2 \omega^4 \,\mathrm{e}^{-\mathrm{i}k\, r_{ij}^{hm}(\mathbf{y},\mathbf{y};l,p;l',p')} \\
& \times \mathrm{e}^{-\mathrm{i}k(\|\mathbf{x}_j^{p''} - \mathbf{y}_0\| - \|\mathbf{x}_j^{p'''} - \mathbf{y}_0\| + \|\mathbf{y}_0 - \mathbf{z}_q^{v}\| - \|\mathbf{y}_0 - \mathbf{z}_{q'}^{v'}\|)} \hat{p}_q(\omega) \hat{p}_{q'}^*(\omega) \,\mathrm{d}\omega \Bigg]
\end{aligned} \tag{103}$$

where $r_{ij}^{hm}(\mathbf{y}, \mathbf{y}; l, p, l', p')$ is as defined in (101), α and α' are multi-indices as defined above and C_1', C_2', C_3' are $i, j, q, q', \alpha, \alpha'$ dependent scaling terms due to geometric spreading factors and multi-path attenuation coefficients. (For explicit definitions of C_1', C_2', C_3' and the derivation of (103), see appendix B.4.)

Similar to (99), the first two terms correspond to the SNR_λ^2 of the true target image due to the direct-path propagation and the multi-path propagation, respectively, while the third term represents the SNR_λ^2 of the artifact component in the reconstructed image.

For $M \geqslant 2$ transmitters and two receivers, the SNR_λ^2 of the true target image increases roughly by a factor of M as compared to the SNR_λ^2 of the two-receiver and a single-transmitter scenario described in (99). As for the SNR_λ^2 of the artifact component, for $M \geqslant 2$ transmitters, the number of summands in the SNR_λ^2 increases roughly by a factor of $M(M+1)/2$. Nevertheless, the strength of the artifact component may be lower than that of the true target, because each summand in the third term is an incoherent (delayed) summation of the

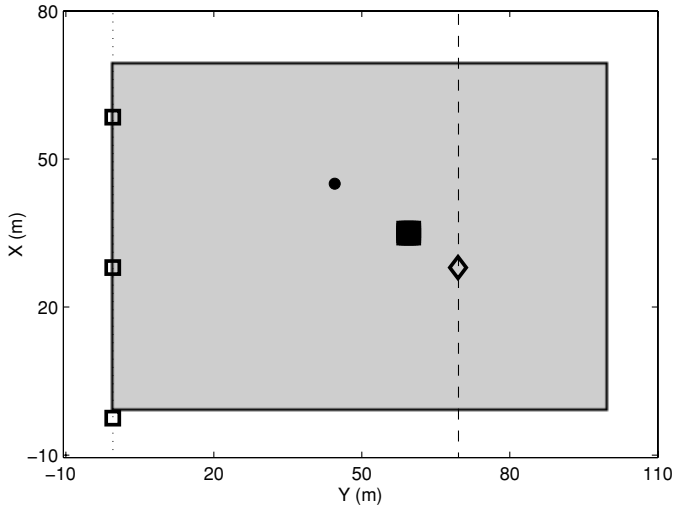

Figure 9. The 2D view of the simulation setup with three receivers and a single transmitter. The gray region denotes the scene considered in all the numerical simulations. The squares along the x-axis show the location of the receivers, and the diamond indicates the location of the transmitter. The black circle indicates the location of the point target and the solid black square shows the extended target.

cross-correlation and auto-correlation of the transmitted waveforms due to the phase term in the summation.

7. Numerical simulations

7.1. Settings

We conducted numerical simulations to verify the theory and to demonstrate the performance of our algorithms using both a point target and an extended target model. For each target model, we conducted simulations for the free-space and multiple-scattering environments with different number of receivers and transmitters.

We assumed that the transmitted signal is continuous wave (CW) with 900 MHz carrier frequency and 10 ns duration. The sampling rate of the signal was chosen to be 5 GHz. For the multiple-transmitter scenario, we assumed that all transmitters are transmitting the same waveform. Note that this corresponds to the least favorable condition due to perfect correlation between the transmitted waveforms.

We consider a scene of size $[0, 70] \times [0, 100]\,\mathrm{m}^2$ with flat topography. We discretized the scene into 140×200 pixels, where $[0\ 0\ 0]^T$ m and $[70\ 100\ 0]^T$ m correspond to the pixels $(1,\ 1)$ and $(140,\ 200)$, respectively. Figure 9 shows the 2D view of the scene with the point target and the extended target projected onto the flat topography. The point target was assumed to be at $[45.34\ 45\ 1]^T$ m with unit reflectivity. The extended target was a square of size $3 \times 3\,\mathrm{m}^2$, which consists of a 7×7 pixel target centered at $[35\ 60\ 1]^T$ m with the uniform reflectivity of 0.1. The squares along the x-axis denote the location of the receivers and the diamond denotes the location of the transmitter. Both the receivers and transmitters were assumed to be located on the same z-plane, $z = 6$, and lie on a straight line, equidistant from each other. The three receivers were located at $[58.8\ 0\ 6]^T$, $[28.3\ 0\ 6]^T$ and $[-2.1\ 0\ 6]^T$, all

in meters. The transmitter was located at $[28.3\ 70\ 6]^T$ m for the single-transmitter case, and $[36.6\ 0\ 6]^T$ m and $[20.1\ 0\ 6]^T$ m for the two-transmitter case.

For the multiple-scattering propagation environment, we considered a specular reflecting wall located at $x = 0$. Thus, the Green's function of the background environment was modeled with the shoot-and-bounce model with one extra path.

In all the experiments, the thermal noise was simulated as the additive white Gaussian process.

For the point target model, we considered the following number of receivers and transmitters: (a) a single transmitter and 3, 5, 10, 20 receivers; (b) 3 receivers and 2, 5 transmitters. 5, 10 and 20 receivers were all assumed to be colinear and evenly distributed on the straight line shown in figure 9 with the x coordinate ranging from -2.1 m to 58.8 m and $y = 0$, $z = 6$. For the extended target model, we only consider the three-receiver and two-transmitter scenario.

For each scenario, we considered both the free-space and multiple-scattering environments. For the point target simulation, we set D_W to a single pixel and for an extended target to a 7×7 pixel window. Note that the regularization of the back-propagation operator was not needed in the simulations due to the nature of the underlying Green's functions.

We define the signal-to-noise ratio of the reconstructed image, SNR_I, as follows:

$$\mathrm{SNR}_I = 20 \log_{10} \frac{|\mathrm{E}[I|\mathcal{H}_1] - \mathrm{E}[I|\mathcal{H}_0]|}{\sqrt{\mathrm{Var}[I|\mathcal{H}_1] + \mathrm{Var}[I|\mathcal{H}_0]}} \tag{104}$$

where I denotes the reconstructed target image. We define the signal-to-noise ratio of the received signal, SNR_m, as

$$\mathrm{SNR}_m = 20 \log_{10} \frac{|\mathrm{E}[m]|}{\sigma_n} \tag{105}$$

where σ_n denotes the standard deviation of the measurements due to additive noise and clutter.

We evaluated the performance of the reconstruction algorithms with respect to the SNR_I of the reconstructed images given the SNR_m of the received signal for different number of transmitters and receivers. We estimated the SNR_I using 20 images, each reconstructed using a different realization of the received signal at a fixed SNR_m. We estimated $\mathrm{E}[I|\mathcal{H}_1]$ by taking a small square area around the target location and averaging the values over all the pixels in the square and over 20 different reconstructions. Similarly, $\mathrm{E}[I|\mathcal{H}_0]$ was estimated by taking a small square section of the background where no target was present. The same method was used to estimate the variances. Note that the SNR_I measures the signal-to-noise ratio of the overall image whereas the SNR_λ^2 measures the signal-to-noise ratio of each pixel.

We computed the SNR_I for different noise levels corresponding to the SNR_m value ranging from -23 dB to 17 dB.

We used a sample average over 20 realizations of measurements to obtain the mean value of the reference measurements.

7.2. Results

Figures 10 and 11 show the reconstructed images for the point target model in free-space and multi-path environments, respectively. Figure 12 shows the reconstructed images for the extended target model in both free-space and multi-path environments.

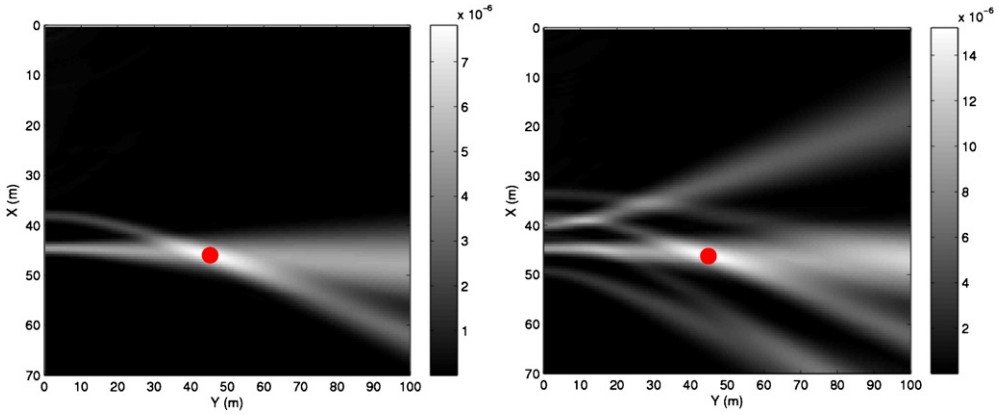

Figure 10. The reconstructed images of a point target in free-space with three receivers and: (a) a single transmitter, and (b) two transmitters. The solid circle shows the true location of the point target.

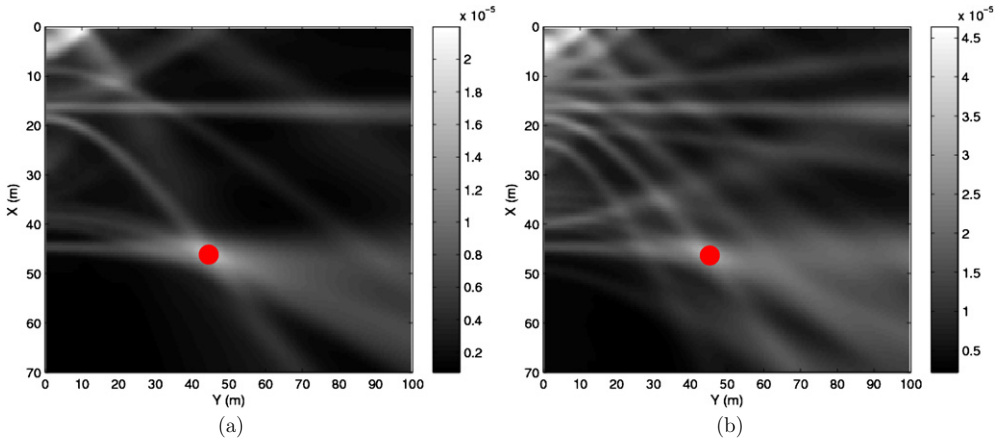

Figure 11. The reconstructed images of a point target in multi-path propagation environments with three receivers and: (a) a single transmitter, and (b) two transmitters. The solid circle shows the true location of the point target.

Comparing figure 10(b) with figure 10(a), and figure 11(b) with figure 11(a), we see that in both free-space and multi-path propagation environments, the strength of the image at the target location increases with the increasing number of transmitters. However, multiple transmitters also induce artifacts in the images due to perfect cross-correlation between the transmitted waveforms as predicted by the theory.

Note that looking at figure 11, we see that the strength of the target increased by almost an order-of-magnitude when we exploited the multi-path effect as compared to the image reconstructed in a free-space propagation environment shown in figure 10. However, there are also additional artifacts as predicted by our discussion in section 6.

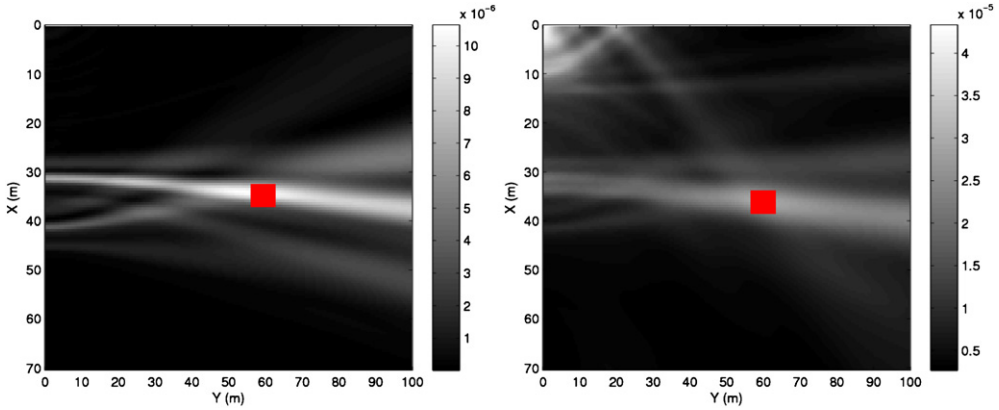

(a) (b)

Figure 12. The reconstructed images of an extended target with three receivers and two transmitters in (a) free-space, and (b) multi-path propagation environments. The solid square shows the true location of the extended target.

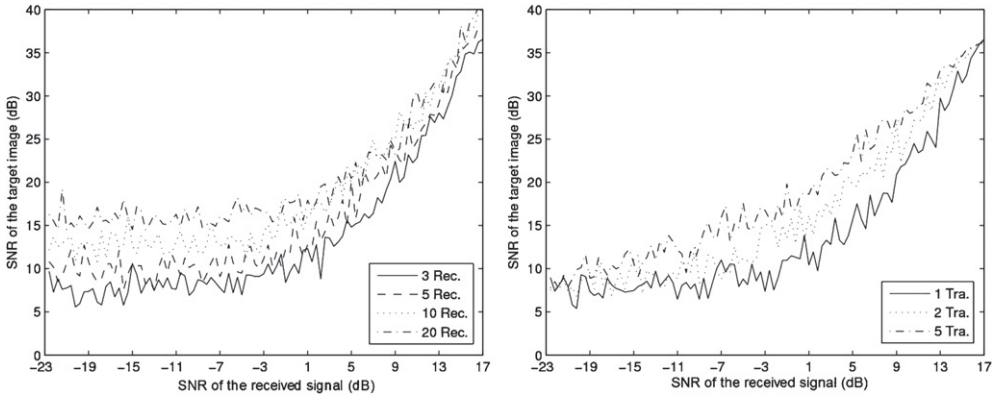

(a) (b)

Figure 13. SNR_I versus SNR_m in free-space for different number of receivers and transmitters: (a) a single transmitter and different number of receivers, and (b) three receivers and different number of transmitters.

Figure 12 shows that the extended target was reconstructed at the correct location in both free-space and multi-path propagation environments. Similar to the analysis of the point-target case, we see that while multi-path scattering and multiple transmitters improve the target strength, they also induce artifacts. Figures 13 and 14 show the SNR_I of the reconstructed images versus the SNR_m for different number of the receivers and transmitters for a point target in free-space and multi-path propagation environments, respectively.

We see that in both free-space and multi-path propagation environments, the SNR_I increases with the increasing number of receivers and transmitters as predicted by the theory. For a low SNR_m, we observe that the SNR_I for the multi-path propagation environments is lower than that of the free-space case even though. Thus, our simulation indicates that the additive noise can have a strong detrimental effect in taking advantage of multi-path scattering in passive imaging.

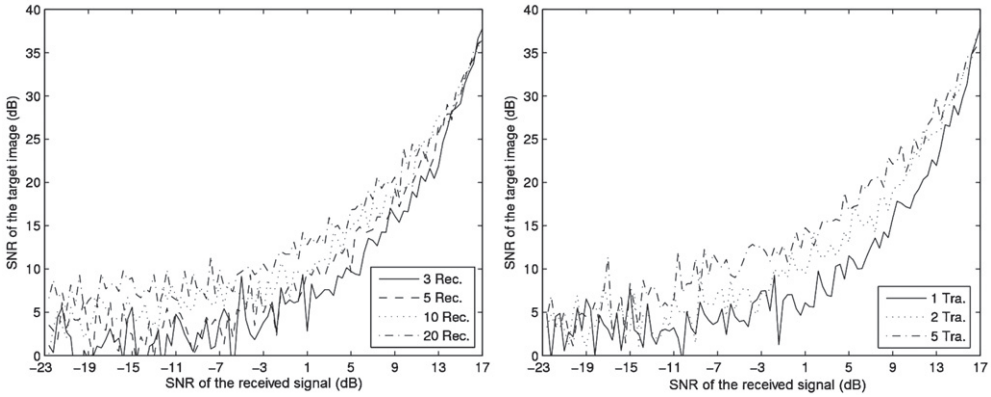

Figure 14. SNR_I versus SNR_m in multi-path propagation environments for different number of receivers and transmitters: (a) a single transmitter and different number of receivers, and (b) three receivers and different number of transmitters.

8. Conclusion

In this work, we presented a new passive image formation method using sparse distributed apertures operating in multiple-scattering environments. The method exploits the multiple scattering and the statistics of the object to be imaged, additive noise and clutter. We first developed a model to relate measurements at a given receiver location to measurements at other receiver locations. This measurement model relies on back-propagating the measurements at a receiver location to a hypothetical target location via the Green's function of the medium and then forward propagating the resulting signal to another receiver location. We next addressed the passive imaging problem within a GLRT framework where we set up a test of binary hypothesis using the measurement model. We designed a linear discriminant functional by maximizing the SNR of the test statistic at each location in the region of interest. The resulting discriminant functional correlates the transformed and filtered measurements from one receiver location with the measurements in another receiver location. The transformation involves the Green's function of the multiple-scattering environment and a spatial windowing function. The filtering involves the statistics of the object to be imaged as well as the additive noise and clutter. We presented the discriminant functional as well as the resulting test statistics for the deterministic and statistical point targets in free-space and multi-path scattering environments for measurements corrupted by noise.

We presented the resolution analysis of our passive imaging algorithm in free-space and multi-path environments. Our analysis shows that in free-space, for a single transmitter and multiple receivers, the PSF of the imaging operator is artifact-free and that the SNR of the image increases linearly with the number of the receivers. However, for multiple transmitters, the PSF of the imaging operator has an artifact component. The strength of the artifact depends on the cross-ambiguity functions of the transmitted waveforms. Using two receivers, the target can be localized up to a certain hyperbola passing through the target location. Using more than two receivers, the target can be localized at the intersection of multiple hyperbolas generated by each pair of receivers.

For the multiple-scattering environment, even for a single transmitter, the reconstructed image is bound to have artifacts due to mirror transmitters. Nevertheless, the strength of the

PSF for the true target location increases by roughly a factor of $(L+1)^3$ where L denotes the number of multi-path bounces. Although the strength of the artifacts increases with the increasing number of background scatterers, due to incoherent summation of the cross-correlation and auto-correlation of the transmitted waveforms, the strength of the resulting artifacts is expected to be smaller than that of the target.

The SNR_λ^2 at the true target location increases cubically with the number of background scatterers, and linearly with the the number of the receivers and transmitters, while the SNR_λ^2 of the artifact components increases linearly with the number of the receivers, but quadratically with the number of the transmitters.

While in this work, we limit ourselves to linear discriminant functionals, the GLRT framework can accommodate non-Gaussian data likelihood and prior models resulting in nonlinear discriminant functionals which may more appropriately represent the probability distribution of the underlying random fields. Within the linear framework, it is also possible to explore alternative design criteria to account for additional constraints or to suppress undesirable artifacts. The investigation of these approaches will be the focus of our future work.

Finally, we note that the passive imaging method introduced in this paper is not limited to radar, and can easily be adapted to similar passive imaging problems in acoustics, geophysics or microwave imaging.

Acknowledgments

The authors would like to thank R Bonneau, M Cheney, T Varslot and C E Yarman for numerous technical discussions. They are grateful to Air Force Office of Scientific Research (AFOSR) for supporting this work under the agreements FA9550-04-1-0223 and FA9550-07-1-0363.

Appendix A. Derivation of the optimal linear template

We begin with the objective functional in (47). The numerator of (47) can be expressed as

$$|\langle \mathbf{G}\overline{\mathbf{m}}_\mathbf{r}, \mathbf{w}\rangle|^2 = \langle \mathbf{G}\overline{\mathbf{m}}_\mathbf{r}, \mathbf{w}\rangle \langle \mathbf{w}, \mathbf{G}\overline{\mathbf{m}}_\mathbf{r}\rangle \tag{A.1}$$

$$= \int \mathbf{w}^H \underbrace{\mathbf{G}\overline{\mathbf{m}}_\mathbf{r}\overline{\mathbf{m}}_\mathbf{r}^H\mathbf{G}^H}_{\mathbf{R}_G} \mathbf{w}\, \mathrm{d}\omega\, \mathrm{d}\omega' \tag{A.2}$$

$$=: \langle \mathcal{R}_G\mathbf{w}, \mathbf{w}\rangle \tag{A.3}$$

where $\mathcal{R}_G$ is a non-negative definite symmetric operator with kernel $\mathbf{R}_G$. $J(\mathbf{w})$ is maximized by taking the Fréchet derivative of (47) with respect to $\mathbf{w}$. To do so we apply the chain rule. The Fréchet derivative of $\langle \mathcal{R}\mathbf{w}, \mathbf{w}\rangle$, where $\mathcal{R}$ is some symmetric non-negative definite bounded linear operator, can be obtained by a straightforward application of Gateaux derivative:

$$Df(\mathbf{w}) = \lim_{t\to 0} \frac{\langle \mathcal{R}(\mathbf{w}+t\mathbf{h}), \mathbf{w}+t\mathbf{h}\rangle - \langle \mathcal{R}\mathbf{w}, \mathbf{w}\rangle}{t} \tag{A.4}$$

$$= \langle \mathcal{R}\mathbf{w}, \mathbf{h}\rangle + \langle \mathcal{R}\mathbf{h}, \mathbf{w}\rangle = \langle \mathcal{R}\mathbf{w}, \mathbf{h}\rangle + \overline{\langle \mathcal{R}\mathbf{w}, \mathbf{h}\rangle} \tag{A.5}$$

$$= 2\,\mathrm{Re}\{\langle \mathcal{R}\mathbf{w}, \mathbf{h}\rangle\}. \tag{A.6}$$

The above holds for all $\mathbf{h} \in L^2 \times \mathbb{R}^M$; thus by the Riez–Fréchet theorem, $Df(\mathbf{w}) = 2\Re\{\langle \mathcal{R}\mathbf{w}, \cdot\rangle\}$ is a linear functional on the function space $L^2 \times \mathbb{R}^M$. For simplicity of notation, $\langle \mathcal{R}\mathbf{w}, \cdot\rangle$ will be denoted as $\mathcal{R}\mathbf{w}$.

Using (A.4), the Fréchet derivative of (47) is given by

$$DJ(\mathbf{w}) = \frac{2\,\mathrm{Re}\{\mathcal{R}_G\mathbf{w}\}}{\langle\overline{\mathcal{R}}\mathbf{w},\mathbf{w}\rangle} - \frac{2\,\mathrm{Re}\{\overline{\mathcal{R}}\mathbf{w}\}\langle\mathcal{R}_G\mathbf{w},\mathbf{w}\rangle}{(\langle\overline{\mathcal{R}}\mathbf{w},\mathbf{w}\rangle)^2} \tag{A.7}$$

$$= \frac{2\,\mathrm{Re}\{\mathcal{R}_G\mathbf{w}\} - 2\,\mathrm{Re}\{\overline{\mathcal{R}}\mathbf{w}\}J(\mathbf{w})}{\langle\overline{\mathcal{R}}\mathbf{w},\mathbf{w}\rangle}. \tag{A.8}$$

By setting $DJ(w) = 0$ and manipulating, we get the following generalized eigenvalue problem:

$$\mathcal{R}_G\mathbf{w} = J(\mathbf{w})\overline{\mathcal{R}}\mathbf{w}. \tag{A.9}$$

By the form of $\mathbf{R}_G$, defined in (A.2), the eigenfunction of $\mathcal{R}_G$ is proportional to $\mathbf{G}\overline{\mathbf{m}}_\mathbf{r}$ and so, assuming $\overline{\mathcal{R}}$ is invertible, the optimal linear detector is proportional to

$$\mathbf{w}_{\mathrm{opt}} = \overline{\mathcal{R}}^{-1}\mathbf{G}\overline{\mathbf{m}}_\mathbf{r}. \tag{A.10}$$

Appendix B. Resolution analysis

B.1. The PSF in free-space for multiple receivers and multiple transmitters

We assume there are $N \geqslant 2$ receivers and $M \geqslant 1$ transmitters in the scene. From (75), (76) and (54), we obtain

$$\mathrm{E}[\hat{m}_i(\omega)] = -T\omega^2\frac{\mathrm{e}^{-\mathrm{i}k\|\mathbf{x}_i-\mathbf{y}_0\|}}{\|\mathbf{x}_i-\mathbf{y}_0\|}\sum_{q=1}^{M}\frac{\mathrm{e}^{-\mathrm{i}k\|\mathbf{y}_0-\mathbf{z}_q\|}}{\|\mathbf{y}_0-\mathbf{z}_q\|}\hat{p}_q(\omega) \tag{B.1}$$

where $\mathbf{x}_i$ $(i = 1,\ldots,N)$ is the location of the ith receiver and p_q is the transmitted waveform of a transmitter located at $\mathbf{z}_q$, $(q = 1,\ldots,M)$.

Using (37), (57) and (B.1), we obtain

$$\begin{aligned}
K(\mathbf{y},\mathbf{y}_0) &= \sum_{i\neq j}^{N}\int w_i\mathrm{E}[\hat{m}_i^*(\omega)]\,\mathrm{d}\omega \\
&= T^2\sum_{q,q'=1}^{M}\sum_{i\neq j}^{N}\frac{\|\mathbf{x}_j-\mathbf{y}\|}{(4\pi)^4\|\mathbf{x}_j-\mathbf{y}_0\|\|\mathbf{x}_i-\mathbf{y}\|\|\mathbf{x}_i-\mathbf{y}_0\|\|\mathbf{y}_0-\mathbf{z}_q\|\|\mathbf{y}_0-\mathbf{z}_{q'}\|} \\
&\quad\times\int\overline{S}_i^{-1}(\omega)\omega^4\,\mathrm{e}^{-\mathrm{i}k\,[r_{ij}^h(\mathbf{y},\mathbf{y}_0)+(\|\mathbf{y}_0-\mathbf{z}_q\|-\|\mathbf{y}_0-\mathbf{z}_{q'}\|)]}\hat{p}_q(\omega)\hat{p}_{q'}^*(\omega)\,\mathrm{d}\omega \\
&= T^2\sum_{q=1}^{M}\sum_{i\neq j}^{N}\underbrace{\frac{\|\mathbf{x}_j-\mathbf{y}\|}{(4\pi)^4\|\mathbf{x}_j-\mathbf{y}_0\|\|\mathbf{x}_i-\mathbf{y}\|\|\mathbf{x}_i-\mathbf{y}_0\|\|\mathbf{y}_0-\mathbf{z}_q\|^2}}_{C_1} \\
&\quad\times\int\overline{S}_i^{-1}(\omega)\omega^4\,\mathrm{e}^{-\mathrm{i}k\,r_{ij}^h(\mathbf{y},\mathbf{y}_0)}|\hat{p}_q(\omega)|^2\,\mathrm{d}\omega \\
&\quad+T^2\sum_{q\neq q'}^{M}\sum_{i\neq j}^{N}\underbrace{\frac{\|\mathbf{x}_j-\mathbf{y}\|}{(4\pi)^4\|\mathbf{x}_j-\mathbf{y}_0\|\|\mathbf{x}_i-\mathbf{y}\|\|\mathbf{x}_i-\mathbf{y}_0\|\|\mathbf{y}_0-\mathbf{z}_q\|\|\mathbf{y}_0-\mathbf{z}_{q'}\|}}_{C_2} \\
&\quad\times\int\overline{S}_i^{-1}(\omega)\omega^4\,\mathrm{e}^{-\mathrm{i}k\,[r_{ij}^h(\mathbf{y},\mathbf{y}_0)+(\|\mathbf{y}_0-\mathbf{z}_q\|-\|\mathbf{y}_0-\mathbf{z}_{q'}\|)]}\hat{p}_q(\omega)\hat{p}_{q'}^*(\omega)\,\mathrm{d}\omega
\end{aligned} \tag{B.2}$$

where

$$r_{ij}^{h}(\mathbf{y},\mathbf{y}_0) = \|\mathbf{x}_i - \mathbf{y}\| - \|\mathbf{x}_j - \mathbf{y}\| + \|\mathbf{x}_j - \mathbf{y}_0\| - \|\mathbf{x}_i - \mathbf{y}_0\| \tag{B.3}$$

and $\mathbf{x}_j$ is the location of the reference receiver.

B.2. SNR_λ *in free-space for multiple receivers and multiple transmitters*

The SNR_λ is calculated according to (39). From (40) and (27), we obtain

$$\mathrm{E}[\lambda|\mathcal{H}_1] - \mathrm{E}[\lambda|\mathcal{H}_0] = \sum_{i\neq j}^{N} \int w_i^j \left(\mathcal{G}_{y,i}\mathcal{G}_{y,j}^{-1}\right)^* \mathrm{E}[\hat{m}_j^*(\omega)]\,\mathrm{d}\omega. \tag{B.4}$$

From (54), for a point target model, we can obtain

$$\mathcal{G}_{y,i}\mathcal{G}_{y,j}^{-1} = \frac{\hat{g}(\mathbf{x}_i,\boldsymbol{y},\omega)}{\hat{g}(\mathbf{x}_j,\boldsymbol{y},\omega)} = \frac{\|\mathbf{x}_j - \mathbf{y}\|}{\|\mathbf{x}_i - \mathbf{y}\|}\,\mathrm{e}^{-\mathrm{i}k(\|\mathbf{x}_i-\mathbf{y}\|-\|\mathbf{x}_j-\mathbf{y}\|)}. \tag{B.5}$$

Using (51) and (B.5), we obtain

$$w_i = \overline{S}_i^{-1}(\omega)\frac{\|\mathbf{x}_j - \mathbf{y}\|}{\|\mathbf{x}_i - \mathbf{y}\|}\,\mathrm{e}^{-\mathrm{i}k(\|\mathbf{x}_i-\mathbf{y}\|-\|\mathbf{x}_j-\mathbf{y}\|)}\mathrm{E}[\hat{m}_j(\omega)]. \tag{B.6}$$

Inserting (B.6) and (B.5) into (B.4), we obtain

$$\mathrm{E}[\lambda|\mathcal{H}_1] - \mathrm{E}[\lambda|\mathcal{H}_0] = \sum_{i\neq j}^{N} \frac{\|\mathbf{x}_j - \mathbf{y}\|^2}{\|\mathbf{x}_i - \mathbf{y}\|^2} \int \overline{S}_i^{-1}(\omega)|\mathrm{E}[\hat{m}_j(\omega)]|^2\,\mathrm{d}\omega. \tag{B.7}$$

From (44) and (B.5), for the deterministic point target and under the assumption that the measurements due to clutter and noise are wide-sense stationary and uncorrelated, we can obtain

$$\begin{aligned}\mathrm{Var}[\lambda|\mathcal{H}_1] + \mathrm{Var}[\lambda|\mathcal{H}_0] &= \int \mathbf{w}^H\left(\mathbf{G}_y\mathbf{R}_\mathbf{n}\mathbf{G}_y^H + 2\mathbf{R}_\mathbf{n}\right)\mathbf{w}\,\mathrm{d}\omega \\ &= 2\sum_{i\neq j}^{N}\int \overline{S}_i(\omega)|w_i(\omega)|^2\,\mathrm{d}\omega.\end{aligned} \tag{B.8}$$

Inserting (B.6) into (B.8) and using (56), (B.8) is expressed as

$$\mathrm{Var}[\lambda|\mathcal{H}_1] + \mathrm{Var}[\lambda|\mathcal{H}_0] = 2\sum_{i\neq j}^{N} \frac{\|\mathbf{x}_j - \mathbf{y}\|^2}{\|\mathbf{x}_i - \mathbf{y}\|^2} \int \overline{S}_i^{-1}(\omega)|\mathrm{E}[\hat{m}_j(\omega)]|^2\,\mathrm{d}\omega. \tag{B.9}$$

Thus, inserting (B.7) and (B.9) into (39), the square of the SNR_λ is given by

$$\mathrm{SNR}_\lambda^2 = \sum_{i\neq j}^{N} \frac{\|\mathbf{x}_j - \mathbf{y}\|^2}{\|\mathbf{x}_i - \mathbf{y}\|^2} \int \overline{S}_i^{-1}(\omega)|\mathrm{E}[\hat{m}_j(\omega)]|^2\,\mathrm{d}\omega. \tag{B.10}$$

Using (B.1) for the measurement at the ith receiver, (B.10) can be expressed by

$$\begin{aligned}\mathrm{SNR}_\lambda^2 &= T^2\sum_{q,q'=1}^{M}\sum_{i\neq j}^{N}\frac{\|\mathbf{x}_j - \mathbf{y}\|^2}{(4\pi)^4\|\mathbf{x}_j - \mathbf{y}_0\|^2\|\mathbf{x}_i - \mathbf{y}\|^2\|\mathbf{y}_0 - \mathbf{z}_q\|\,\|\mathbf{y}_0 - \mathbf{z}_{q'}\|} \\ &\quad\times\int \overline{S}_i^{-1}(\omega)\omega^4\,\mathrm{e}^{-\mathrm{i}k(\|\mathbf{y}_0-\mathbf{z}_q\|-\|\mathbf{y}_0-\mathbf{z}'_q\|))}\,\hat{p}_q(\omega)\,\hat{p}_{q'}^*(\omega)\,\mathrm{d}\omega \\ &= T^2\sum_{q=1}^{M}\sum_{i\neq j}^{N}\underbrace{\frac{\|\mathbf{x}_j - \mathbf{y}\|^2}{(4\pi)^4\|\mathbf{x}_j - \mathbf{y}_0\|^2\|\mathbf{x}_i - \mathbf{y}\|^2\|\mathbf{y}_0 - \mathbf{z}_q\|^2}}_{C_1'}\int \overline{S}_i^{-1}(\omega)\omega^4|\hat{p}_q(\omega)|^2\,\mathrm{d}\omega\end{aligned}$$

$$+T^2\sum_{q\neq q'}^{M}\sum_{i\neq j}^{N}\underbrace{\frac{\|\mathbf{x}_j-\mathbf{y}\|^2}{(4\pi)^4\|\mathbf{x}_j-\mathbf{y}_0\|^2\|\mathbf{x}_i-\mathbf{y}\|^2\|\mathbf{y}_0-\mathbf{z}_q\|\|\mathbf{y}_0-\mathbf{z}_{q'}\|}}_{C_2'}$$

$$\times\int\overline{S}_i^{-1}(\omega)\omega^4\,\mathrm{e}^{-\mathrm{i}k(\|\mathbf{y}_0-\mathbf{z}_q\|-\|\mathbf{y}_0-\mathbf{z}_q'\|)}\hat{p}_q(\omega)\hat{p}_{q'}^*(\omega)\,\mathrm{d}\omega. \tag{B.11}$$

B.3. The PSF in multi-path environments for multiple receivers and multiple transmitters

Assuming that there are $N\geqslant 2$ receivers and $M\geqslant 1$ transmitters, from (75), (76) and (89), we obtain

$$\mathrm{E}[\hat{m}_i(\omega)]=-T\omega^2\sum_{q=1}^{M}\sum_{l,\nu=0}^{L}a_l a_\nu\frac{\mathrm{e}^{-\mathrm{i}k(\|\mathbf{x}_i^l-\mathbf{y}_0\|+\|\mathbf{y}_0-\mathbf{z}_q^\nu\|)}}{(4\pi)^2\|\mathbf{x}_i^l-\mathbf{y}_0\|\|\mathbf{y}_0-\mathbf{z}_q^\nu\|}\hat{p}_q(\omega) \tag{B.12}$$

where $\mathbf{z}_q^0=\mathbf{z}_q\,(q=1,\ldots,M)$, which denote the location of the real transmitter, and $\mathbf{z}_q^\nu\,(\nu=1,\ldots,L)$ denote the location of the mirror transmitters corresponding to the qth transmitter for the νth multi-bounce. L denotes the number of the multi-bounces in the environments.

Using (37), (91), (93) and (B.12), we obtain

$$\begin{aligned}K(\mathbf{y},\mathbf{y}_0)&=\sum_{i\neq j}^{N}\int w_i\mathrm{E}[\hat{m}_i^*(\omega)]\,\mathrm{d}\omega\\&=T^2\sum_{q,q'=1}^{M}\sum_{i\neq j}^{N}\sum_{l,p,l',p',\nu,\nu'=0}^{L}\\&\quad\times\frac{a_l a_p a_{l'}a_{p'}a_\nu a_{\nu'}}{(4\pi)^6\|\mathbf{x}_i^l-\mathbf{y}\|\|\mathbf{x}_j^p-\mathbf{y}\|\|\mathbf{x}_i^{l'}-\mathbf{y}_0\|\|\mathbf{x}_j^{p'}-\mathbf{y}_0\|\|\mathbf{y}_0-\mathbf{z}_q^\nu\|\|\mathbf{y}_0-\mathbf{z}_{q'}^{\nu'}\|}\\&\quad\times\int\overline{S}_i^{-1}(\omega)\tilde{H}_j(\omega)\omega^4\,\mathrm{e}^{-\mathrm{i}k\,[r_{ij}^{hm}(\mathbf{y},\mathbf{y}_0;l,p,l',p')+(\|\mathbf{y}_0-\mathbf{z}_q^\nu\|-\|\mathbf{y}_0-\mathbf{z}_{q'}^{\nu'}\|)]}\hat{p}_q(\omega)\hat{p}_{q'}^*(\omega)\,\mathrm{d}\omega\end{aligned} \tag{B.13}$$

$$\begin{aligned}&=T^2\sum_{q=1}^{M}\sum_{i\neq j}^{N}\sum_{l,p,\nu=0}^{L}\underbrace{\frac{a_l^2a_p^2a_\nu^2}{\|\mathbf{x}_i^l-\mathbf{y}\|\|\mathbf{x}_j^p-\mathbf{y}\|\|\mathbf{x}_i^l-\mathbf{y}_0\|\|\mathbf{x}_j^p-\mathbf{y}_0\|\|\mathbf{y}_0-\mathbf{z}_q^\nu\|^2}}_{C_1}\\&\quad\times\int\overline{S}_i^{-1}(\omega)\tilde{H}_j(\omega)\omega^4\,\mathrm{e}^{-\mathrm{i}k\,r_{ij}^{hm}(\mathbf{y},\mathbf{y}_0;l,p;l,p)}|\hat{p}_q(\omega)|^2\,\mathrm{d}\omega+T^2\sum_{q\neq q'}^{M}\sum_{i\neq j}^{N}\sum_{l\neq l',p\neq p',\nu\neq\nu'}^{L}\\&\quad\times\underbrace{\frac{a_l a_p a_{l'}a_{p'}a_\nu a_{\nu'}}{(4\pi)^6\|\mathbf{x}_i^l-\mathbf{y}\|\|\mathbf{x}_j^p-\mathbf{y}\|\|\mathbf{x}_i^{l'}-\mathbf{y}_0\|\|\mathbf{x}_j^{p'}-\mathbf{y}_0\|\|\mathbf{y}_0-\mathbf{z}_q^\nu\|\|\mathbf{y}_0-\mathbf{z}_{q'}^{\nu'}\|}}_{C_2}\\&\quad\times\int\overline{S}_i^{-1}(\omega)\tilde{H}_j(\omega)\omega^4\,\mathrm{e}^{-\mathrm{i}k\,[r_{ij}^{hm}(\mathbf{y},\mathbf{y}_0;l,p,l',p')+(\|\mathbf{y}_0-\mathbf{z}_q^\nu\|-\|\mathbf{y}_0-\mathbf{z}_{q'}^{\nu'}\|)]}\hat{p}_q(\omega)\hat{p}_{q'}^*(\omega)\,\mathrm{d}\omega\end{aligned} \tag{B.14}$$

where

$$r_{ij}^{hm}(\mathbf{y},\mathbf{y}_0;l,p;l',p')=\|\mathbf{x}_i^l-\mathbf{y}\|-\|\mathbf{x}_j^p-\mathbf{y}\|+\|\mathbf{x}_j^{p'}-\mathbf{y}_0\|-\|\mathbf{x}_i^{l'}-\mathbf{y}_0\| \tag{B.15}$$

and

$$r_{ij}^{hm}(\mathbf{y}, \mathbf{y}_0; l, p; l, p) = \left\|\mathbf{x}_i^l - \mathbf{y}\right\| - \left\|\mathbf{x}_j^p - \mathbf{y}\right\| + \left\|\mathbf{x}_j^p - \mathbf{y}_0\right\| - \left\|\mathbf{x}_i^l - \mathbf{y}_0\right\|. \tag{B.16}$$

For the case there are only two receivers and a single transmitter, (B.13) reduces to

$$K(\mathbf{y}, \mathbf{y}_0) = T^2 \sum_{l,p,l',p',\nu,\nu'=0}^{L} \underbrace{\frac{a_l a_p a_{l'} a_{p'} a_\nu a_{\nu'}}{(4\pi)^6 \left\|\mathbf{x}_2^l - \mathbf{y}\right\| \left\|\mathbf{x}_1^p - \mathbf{y}\right\| \left\|\mathbf{x}_2^{l'} - \mathbf{y}_0\right\| \left\|\mathbf{x}_1^{p'} - \mathbf{y}_0\right\| \left\|\mathbf{y}_0 - \mathbf{z}_1^\nu\right\| \left\|\mathbf{y}_0 - \mathbf{z}_1^{\nu'}\right\|}}_{C}$$
$$\times \int \overline{S}_2^{-1}(\omega) \tilde{H}_1(\omega) \omega^4 \, \mathrm{e}^{-\mathrm{i}k\,[r_{21}^{hm}(\mathbf{y},\mathbf{y}_0;l,p,l',p') + (\|\mathbf{y}_0 - \mathbf{z}_1^\nu\| - \|\mathbf{y}_0 - \mathbf{z}_1^{\nu'}\|)]} |\hat{p}_1(\omega)|^2 \, \mathrm{d}\omega. \tag{B.17}$$

B.4. SNR_λ *in multi-path environments for multiple receivers and multiple transmitters*

From (40), (44), (51), (27) and (89), for the deterministic point targets and under the assumption that the measurements due to clutter and noise are wide-sense stationary and uncorrelated, we can obtain

$$\mathrm{E}[\lambda|\mathcal{H}_1] - \mathrm{E}[\lambda|\mathcal{H}_0] = \sum_{i\neq j}^{N} \int \overline{S}_i^{-1}(\omega) |\tilde{D}_{ij}(\omega)|^2 |\mathrm{E}[\hat{m}_j(\omega)]|^2 \, \mathrm{d}\omega, \tag{B.18}$$

$$\frac{1}{2}[\mathrm{Var}[\lambda|\mathcal{H}_1] + \mathrm{Var}[\lambda|\mathcal{H}_0]] = \sum_{i\neq j}^{N} \int \overline{S}_i^{-1}(\omega) |\tilde{D}_{ij}(\omega)|^2 |\mathrm{E}[\hat{m}_j(\omega)]|^2 \, \mathrm{d}\omega \tag{B.19}$$

where $\tilde{D}_{ij}(\omega)$ is given by (93).

Inserting (B.18) and (B.19) into (39), the square of the SNR_λ is then given as follows:

$$\mathrm{SNR}_\lambda^2 = \sum_{i\neq j}^{N} \int \overline{S}_i^{-1}(\omega) |\tilde{D}_{ij}(\omega)|^2 |\mathrm{E}[\hat{m}_j(\omega)]|^2 \, \mathrm{d}\omega. \tag{B.20}$$

Using (93) and (B.12) for the measurement at the jth receiver, (B.20) is expressed by

$$\mathrm{SNR}_\lambda^2 = T^2 \sum_{q,q'=1}^{M} \sum_{i\neq j}^{N} \sum_{\alpha,\alpha'=0}^{L} \frac{a_l a_p a_{l'} a_{p'}}{(4\pi)^8 \|\mathbf{x}_i^l - \mathbf{y}\| \|\mathbf{x}_j^p - \mathbf{y}\| \|\mathbf{x}_i^{l'} - \mathbf{y}\| \|\mathbf{x}_j^{p'} - \mathbf{y}\|}$$
$$\times \frac{a_{p''} a_{p'''} a_\nu a_{\nu'}}{\left\|\mathbf{x}_j^{p''} - \mathbf{y}_0\right\| \left\|\mathbf{x}_j^{p'''} - \mathbf{y}_0\right\| \left\|\mathbf{y}_0 - \mathbf{z}_q^\nu\right\| \left\|\mathbf{y}_0 - \mathbf{z}_{q'}^{\nu'}\right\|} \int \overline{S}_i^{-1}(\omega) |\tilde{H}_j(\omega)|^2 \omega^4$$
$$\times \mathrm{e}^{-\mathrm{i}k\,[r_{ij}^{hm}(\mathbf{y},\mathbf{y};l,p;l',p') + \|\mathbf{x}_j^{p''} - \mathbf{y}_0\| - \|\mathbf{x}_j^{p'''} - \mathbf{y}_0\| + \|\mathbf{y}_0 - \mathbf{z}_q^\nu\| - \|\mathbf{y}_0 - \mathbf{z}_{q'}^{\nu'}\|]} \hat{p}_q(\omega) \hat{p}_{q'}^*(\omega) \, \mathrm{d}\omega \tag{B.21}$$

where $\alpha = (l, p, p'', \nu)$, $\alpha' = (l', p', p''', \nu')$ and $r_{ij}^{hm}(\mathbf{y}, \mathbf{y}; l, p; l', p')$ is given by (B.15). It can be further written as

$$\mathrm{SNR}_\lambda^2 = T^2 \sum_{q=1}^{M} \sum_{i\neq j}^{N} \underbrace{\frac{1}{(4\pi)^8 \|\mathbf{x}_i - \mathbf{y}\|^2 \|\mathbf{x}_j - \mathbf{y}\|^2 \|\mathbf{x}_j - \mathbf{y}_0\|^2 \|\mathbf{y}_0 - \mathbf{z}_q\|^2}}_{C_1'}$$
$$\times \int \overline{S}_i^{-1}(\omega) |\tilde{H}_j(\omega)|^2 \omega^4 |\hat{p}_q(\omega)|^2 \, \mathrm{d}\omega$$

$$+T^2\sum_{q=1}^{M}\sum_{i\neq j}^{N}\sum_{l,p,v\neq 0}^{L}\underbrace{\frac{a_l^2a_p^2a_v^2}{\left\|\mathbf{x}_i^l-\mathbf{y}\right\|^2\left\|\mathbf{x}_j^p-\mathbf{y}\right\|^2\left\|\mathbf{x}_j^p-\mathbf{y}_0\right\|^2\left\|\mathbf{y}_0-\mathbf{z}_q^v\right\|^2}}_{C_2'}$$

$$\times\int\overline{S}_i^{-1}(\omega)|\tilde{H}_j(\omega)|^2\omega^4|\hat{p}_q(\omega)|^2\,\mathrm{d}\omega$$

$$+T^2\sum_{q\neq q'}^{M}\sum_{i\neq j}^{N}\sum_{\alpha\neq\alpha'}^{L}2\,C_3'\,\mathrm{Re}\left[\int\overline{S}_i^{-1}(\omega)|\tilde{H}_j(\omega)|^2\omega^4\right.$$

$$\left.\times\,\mathrm{e}^{-\mathrm{i}k\,[r_{ij}^{hm}(\mathbf{y},\mathbf{y};l,p;l',p')+\|\mathbf{x}_j^{p''}-\mathbf{y}_0\|-\|\mathbf{x}_j^{p'''}-\mathbf{y}_0\|+\|\mathbf{y}_0-\mathbf{z}_q^v\|-\|\mathbf{y}_0-\mathbf{z}_{q'}^{v'}\|]}\hat{p}_q(\omega)\hat{p}_{q'}^*(\omega)\,\mathrm{d}\omega\right]$$

where

$$C_3'=\frac{a_la_pa_{l'}a_{p'}a_{p''}a_{p'''}a_va_{v'}}{(4\pi)^8\left\|\mathbf{x}_i^l-\mathbf{y}\right\|\left\|\mathbf{x}_j^p-\mathbf{y}\right\|\left\|\mathbf{x}_i^{l'}-\mathbf{y}\right\|\left\|\mathbf{x}_j^{p'}-\mathbf{y}\right\|\left\|\mathbf{x}_j^{p''}-\mathbf{y}_0\right\|\left\|\mathbf{x}_j^{p'''}-\mathbf{y}_0\right\|}\frac{1}{\left\|\mathbf{y}_0-\mathbf{z}_q^v\right\|\left\|\mathbf{y}_0-\mathbf{z}_{q'}^{v'}\right\|}. \tag{B.22}$$

Note that the first two terms of (B.22) correspond to the case where $\alpha=\alpha'$ and $p=p''$, and the third term corresponds to that where $\alpha\neq\alpha'$ and $p\neq p''$.

References

[1] Borcea L, Papanicolaou G and Tsogka C 2006 Coherent interferometric imaging in clutter *Geophysics* **71** SI165–75

[2] Borcea L, Papanicolaou G and Tsogka C 2005 Interferometric array imaging in clutter *Inverse Problems* **21** 1419–60

[3] Adve R, Schneibler R, Genello G and Antonik P 2005 Waveform-space-time adaptive processing for distributed aperture radars *Proc. IEEE Radar Conf. (Arlington, VA, USA, 9–12 May 2005)* pp 93–7

[4] Griffiths H D and Long N R W 1986 Television-based bistatic radar *IEE Proc. F* **133** 649–57

[5] Griffiths H D, Garnett A, Baker C J and Keaveney S 1992 Bistatic radar using satellite-borne illuminators of opportunity *Proc. IEEE Int. Radar Conf. (Brighton, UK, 12–13 October 1992)* pp 276–9

[6] Griffiths H D and Baker C J 2005 Passive coherent location radar systems: Part 1. Performance prediction *IEE Proc. F* **152** 153–9

[7] Baker C J, Griffiths H D and Papoutsis I 2005 Passive coherent location radar systems: Part 2. Waveform properties *IEE Proc. F* **152** 160–8

[8] Howland P E, Maksimiuk D and Reitsma G 2005 Fm radio based bistatic radar *IEE Proc. F* **152** 107–15

[9] Tan D K P, Sun H, Lu Y, Lesturgie M and Chan H L 2005 Passive radar using global system for mobile communication signal: theory, implementation and measurements *IEE Proc. F* **152** 116–23

[10] Koch V and Westphal R 1995 New approach to a multistatic passive radar sensor for air/space defense *IEEE Aerosp. Electron. Syst. Mag.* **10** 24–32

[11] Howland P E 1999 Target tracking using television-based bistatic radar *IEE Proc. F* **146** 166–74

[12] Poullin D 2005 Passive detection using digital broadcasters (DAB, DVB) with COFDM modulation *IEE Proc. F* **152** 143–52

[13] Cherniakov M, Kubik K and Nezlin D 2000 Bistatic synthetic aperture radar with non-cooperative leos based transmitter *Proc. IEEE Int. Geoscience and Remote Sensing Symp. (Honolulu, Hawaii, USA, 24–28 July 2000)* vol 2 pp 861–2

[14] Homer J, Kubik K, Mojarrabi B, Longstaff I, Donskoi E and Cherniakov M 2002 Passive bistatic radar sensing with leos based transmitters *Proc. IEEE Int. Geoscience and Remote Sensing Symp. (Toronto, Canada, 24–28 June 2002)* pp 438–40

[15] Cherniakov M, Saini R, Zuo R and Antoniou M 2005 Space surface bistatic SAR with space-borne non-cooperative transmitters *Proc. Eur. Radar Conf. (Paris, France, 6–7 October 2005)* vol 2 pp 25–8

[16] He X, Cherniakov M and Zeng T 2005 Signal detectability in SS-BSAR with GNSS non-cooperative transmitter *IEE Proc. F* **152** 124–32

[17] Garnier J and Papanicolaou G 2009 Passive sensor imaging using cross correlations of noisy signals in a scattering medium *SIAM J. Imaging Sci* **2** 396–437

[18] Kulpa K S 2005 Multi-static entirely passive detection of moving targets and its limitations *IEE Proc. F* **152** 169–73
[19] Norton S J and Linzer M 1987 Backprojection reconstruction of random source distributions *J. Acoust. Soc. Am.* **81** 977–85
[20] Norton S J, Carr B J and Witten A J 2006 Passive imaging of underground acoustic sources *J. Acoust. Soc. Am.* **119** 2840–7
[21] Yarman C E and Yazıcı B 2008 Synthetic aperture hitchhiker imaging *IEEE Trans. Imaging Process.* **17** 2156–73
[22] Snieder R 2004 Extracting the Green's function from the correlation of coda waves: a derivation based on stationary phase *Phys. Rev.* E **69** 046610–1
[23] Lobkis O I and Weaver R L 2001 On the emergence of the Green's function in the correlations of a diffuse field *J. Acoust. Soc. Am.* **110** 3011–7
[24] Derode A, Larose E, Campillo M and Fink M 2003 Recovering the Green's function from field–field correlations in an open scattering medium (l) *J. Acoust. Soc. Am.* **113** 2973–6
[25] Garnier J 2005 Imaging in randomly layered media by cross-correlating noisy signals *SIAM J. Multiscale Model. Simul.* **4** 610–40
[26] Derveaux G, Papanicolaou G and Tsogka C 2007 Time reversal imaging for sensor networks with optimal compensation in time *J. Acoust. Soc. Am* **121** 2071–85
[27] Bonneau R J 2005 A rate distortion method for waveform design in RF image formation *Proc. 34th Applied Imagery and Pattern Recognition Workshop (Washington DC, USA, 19–21 October 2005)* pp 63–9
[28] Bonneau R J 2006 A rate distortion method for waveform design in RF target detection *Aerospace Conf. 2006 IEEE (Big Sky, MT, USA, 4–11 March)* pp 1–12
[29] Bonneau R J 2006 A waveform strategy for detection of targets in multiplicative clutter *Proc. 2006 IEEE Radar Conference (Verona, NY, USA, 24–27 April)* pp 84–93
[30] Attia E H and Steinberg B D 1989 Self-cohering large antenna arrays using the spatial correlation properties of radar clutter *IEEE Trans. Antennas Propag.* **37** 30–8
[31] Cherniakov M, Kubik K and Nezlin D 2000 Radar sensors based on communication low earth orbiting satellites microwave emission *IEEE Trans. Geosci. Remote Sens.* **2** 1007–8
[32] Borcea L, Papanicolaou G and Tsogka C 2003 Theory and applications of time reversal and interferometric imaging *Inverse Problems* **19** S139–64
[33] Kay S 1993 *Fundamentals of Statistical Signal Processing: Vol. I. Estimation Theory* (Englewood Cliffs, NJ: Prentice Hall)
[34] Kay S 1998 *Fundamentals of Statistical Signal Processing: Vol II. Detection Theory* (Englewood Cliffs, NJ: Prentice Hall)
[35] Voccola K, Yazici B, Cheney M and Ferrara M 2009 On the equivalence of the generalized likelihood ratio test and backprojection method in synthetic aperture imaging *Proc. SPIE Conf. of Defense, Security and Sensing (Orlando, FL, USA, 13–17 April 2009)* vol 7335 pp 1–10
[36] Colton D and Kress R 1998 *Inverse Acoustic and Electromagnetic Scattering Theory (Applied Mathematical Sciences* vol 93*)* 2nd edn (Berlin: Springer)
[37] Ghosh Roy D N and Couchman L S 2002 *Inverse Problems and Inverse Scattering of Plane Waves* (London, UK: Academic)
[38] Barrett H H and Myers K J 2003 *Foundations of Image Science* (New York: Wiley Interscience)
[39] Cheney M 2001 A mathematical tutorial on synthetic aperture radar *SIAM Rev.* **43** 301–12
[40] Van Veen B D and Buckley K M 1988 Beamforming: a versatile approach to spatial filtering *IEEE Acoust. Speech Signal Process. Mag.* **5** 4–24
[41] Varslot T, Yazici B and Cheney M 2008 Wide band pulse-echo imaging with distributed apertures in multi-path environments *Inverse Problems* **24** 1–28
[42] Haimovich A M, Blum R S and Cimini L J 2008 Mimo radar with widely separated antennas *IEEE Signal Process. Mag.* **25** 116–29
[43] Van Trees H L 2001 *Detectaion, Estimation and Modulation Theory: I. Detection, Estimation, and Linear Modulation Theory* vol 1 (New York: Wiley Interscience)
[44] Born M and Wolf E 1999 *Principles of Optics* 7th edn (Cambridge: Cambridge University Press)
[45] Bleistein N, Cohen J K and Stockwell J W 2001 *Mathematics of Multi-dimensional Seismic Imaging, Migration and Inversion, Interdisciplinary Applied Mathematics* (Berlin: Springer)
[46] Kwon K and Yazici B 2010 Born expansion and Frechet derivatives in non-linear diffuse optical tomography *Comput. Math. Appl.* (accepted)
[47] Lax M 1951 Multiple scattering of waves *Rev. Mod. Phys.* **23** 287–310
[48] Chew W C 1990 *Waves and Fields in Inhomogeneous Media* (New York: IEEE Press)
[49] Skolnik M I 2008 *Introduction to Radar Systems* 3rd edn (New York: McGraw-Hill)
[50] Cook C E and Bernfeld M 1967 *Radar Signals* (New York: Academic)